Monthly Notices of the ROYAL ASTRONOMICAL SOCIETY

MNRAS **459,** 1626–1645 (2016) doi:10.1093/mnras/stw712
Advance Access publication 2016 March 28

A complete census of *Herschel*-detected infrared sources within the *HST* Frontier Fields

T. D. Rawle,[1,2★] B. Altieri,[1] E. Egami,[3] P. G. Pérez-González,[4] F. Boone,[5] B. Clement,[6] R. J. Ivison,[7,8] J. Richard,[6] W. Rujopakarn,[9,10] I. Valtchanov,[1] G. Walth,[3] B. J. Weiner,[3] A. W. Blain,[11] M. Dessauges-Zavadsky,[12] J.-P. Kneib,[13] D. Lutz,[14] G. Rodighiero,[15] D. Schaerer[5,12] and I. Smail[16]

[1]*European Space Astronomy Centre (ESA/ESAC), Science Operations Department, E-28691 Villanueva de la Cañada, Madrid, Spain*
[2]*ESA/Space Telescope Science Institute (STScI), 3700 San Martin Drive, Baltimore, MD 21218, USA*
[3]*Steward Observatory, University of Arizona, 933 N. Cherry Ave, Tucson, AZ 85721, USA*
[4]*Departamento de Astrofísica, Facultad de CC. Físicas,Universidad Complutense de Madrid, E-28040 Madrid, Spain*
[5]*Université de Toulouse, UPS-OMP, CNRS, IRAP, 9 Av. colonel Roche, BP 44346, F-31028 Toulouse Cedex 4, France*
[6]*Univ Lyon, Univ Lyon1, Ens de Lyon, CNRS, Centre de Recherche Astrophysique de Lyon UMR5574, F-69230 Saint-Genis-Laval, France*
[7]*European Southern Observatory, Karl-Schwarzschild-Str. 2, D-85748 Garching bei München, Germany*
[8]*Institute for Astronomy, University of Edinburgh, Royal Observatory, Blackford Hill, Edinburgh EH9 3HJ, UK*
[9]*Department of Physics, Faculty of Science, Chulalongkorn University, 254 Phayathai Road, Pathumwan, Bangkok 10330, Thailand*
[10]*Kavli Institute for the Physics and Mathematics of the Universe (WPI), The University of Tokyo Institutes for Advanced Study, The University of Tokyo, Kashiwa, Chiba 277-8583, Japan*
[11]*Department of Physics and Astronomy, University of Leicester, University Road, Leicester LE1 7RH, UK*
[12]*Observatoire de Genève, Université de Genève, 51 Ch. des Maillettes, CH-1290 Sauverny, Switzerland*
[13]*Laboratoire d'Astrophysique EPFL, Observatoire de Sauverny, Versoix, CH-1290 Switzerland*
[14]*Max-Planck-Institut für extraterrestrische Physik, Postfach 1312, Giessenbachstrasse 1, D-85741 Garching, Germany*
[15]*Dipartimento di Fisica e Astronomia 'Galileo Galilei', Universitá di Padova, Vicolo dell'Osservatorio, 3, I-35122 Padova, Italy*
[16]*Centre for Extragalactic Astronomy, Department of Physics, Durham University, South Road, Durham DH1 3LE, UK*

Accepted 2016 March 23. Received 2016 February 20; in original form 2015 August 3

ABSTRACT

We present a complete census of all *Herschel*-detected sources within the six massive lensing clusters of the *HST* Frontier Fields (HFF). We provide a robust legacy catalogue of 263 sources with *Herschel* fluxes, primarily based on imaging from the *Herschel Lensing Survey* and PEP/HerMES Key Programmes. We optimally combine *Herschel*, *Spitzer* and *WISE* infrared (IR) photometry with data from *HST*, VLA and ground-based observatories, identifying counterparts to gain source redshifts. For each *Herschel*-detected source we also present magnification factor (μ), intrinsic IR luminosity and characteristic dust temperature, providing a comprehensive view of dust-obscured star formation within the HFF. We demonstrate the utility of our catalogues through an exploratory overview of the magnified population, including more than 20 background sub-LIRGs unreachable by *Herschel* without the assistance gravitational lensing.

Key words: galaxies: star formation – infrared: galaxies – submillimetre: galaxies.

1 INTRODUCTION

The *Hubble Space Telescope* (*HST*) Frontier Fields (HFF)[1] is an ongoing programme (2013–2016) to obtain ultradeep imaging of six intermediate-redshift galaxy clusters, using 840 orbits of Director's Discretionary Time (PI: Lotz; Lotz et al., in preparation). The primary goal is to exploit the gravitational lensing effect of these massive foreground structures to study background galaxies in the very early Universe. HFF employs both the Advanced Camera for Surveys (ACS) and the Wide Field Camera 3 (WFC3) to gain imaging throughout the rest-frame optical and near-infrared (NIR). Although the observations are intrinsically shallower than e.g. the *Hubble Extremely Deep Field* (XDF; Illingworth et al. 2013), the additional effective depth yielded by the wide-scale cluster lensing provides a first glimpse of the galaxy population to be probed in detail by the *James Webb Space Telescope* (*JWST*).

★ E-mail: tim.rawle@sciops.esa.int
[1] http://www.stsci.edu/hst/campaigns/frontier-fields/

Table 1. Summary of the HFF central (C) and parallel (P) footprints, including available imaging. Positions are the nominal *HST* pointing and redshift (z) is for the target cluster. Coverage is tabulated for SPIRE (S), PACS (PPP = 70+100+160 μm), MIPS 24 μm (M), IRAC (IIII = channels 1–4), *WISE* (W), *HST* (H; * for complete HFF imaging at the time of writing), VLA (V). This table is representative only: partial coverage may result in fewer available bands at the footprint extremities.

Cluster	z		RA	Dec	Coverage...						
A2744	0.308	C	00:14:21.2	–30:23:50.1	S	–PP	M	IIII	W	H*	–
		P	00:13:53.6	–30:22:54.3	S	–	–	–	W	H*	–
A370	0.375	C	02:39:52.9	–01:34:36.5	S	–PP	M	IIII	W	H	V
		P	02:40:13.4	–01:37:32.8	S	–	M	II–	W	–	V
MACSJ0416.1–2403 (M0416)	0.396	C	04:16:08.9	–24:04:28.7	S	–PP	–	II–	W	H*	V
		P	04:16:33.1	–24:06:48.7	S	–	–	–	W	H*	V
MACSJ0717.5+3745 (M0717)	0.545	C	07:17:34.0	+37:44:49.0	S	–PP	M	IIII	W	H*	V
		P	07:17:17.0	+37:49:47.3	S	–	M	IIII	W	H*	V
MACSJ1149.5+2223 (M1149)	0.543	C	11:49:36.3	+22:23:58.1	S	PPP	–	II–	W	H	V
		P	11:49:40.5	+22:18:02.3	S	–	–	II–	W	H	V
RXCJ2248.7–4431 (AS1063)	0.348	C	22:48:44.4	–44:31:48.5	S	PPP	M	IIII	W	H	–
		P	22:49:17.7	–44:32:43.8	S	–	–	I–	W	–	–

HFF comprises six clusters chosen primarily for their predicted lensing strength, low zodiacal background and observability by large ground-based facilities (e.g. ALMA, VLT and/or those on Mauna Kea). The ACS/WFC3 parallel mode provides two distinct footprints per cluster. A central field is aligned with the highest magnification cluster core, while the parallel location is constrained by guide star availability and selected to maximize image quality (i.e. avoiding bright stars). HFF includes two northern and four southern clusters, covering a range of Right Ascension and redshifts within $z \sim 0.30$–0.55 (see Table 1).

Rest-frame optical and NIR imaging probes the unobscured evolved stellar component of extragalactic sources. An understanding of the processes governing star formation is required to answer fundamental questions concerning galaxy evolution. Much of the star formation activity in the Universe is shrouded in dust (see the review, Casey, Narayanan & Cooray 2014), giving an imprint of star formation characteristics on the recycled light in the far-infrared (FIR). The *Herschel Space Observatory* (Pilbratt et al. 2010) was launched in 2009 with the specific goal of understanding galaxy dust and obscured star formation. By the mission end in 2013, *Herschel* had obtained more than 25 000 h of FIR data.

Herschel large-area surveys of well-studied extragalactic fields have provided a new understanding of dust temperature (e.g. Hwang et al. 2010; Magnelli et al. 2014), dust mass (Rowlands et al. 2014; Santini et al. 2014) and spectral energy distribution (SED) shape (Berta et al. 2013) in IR/submillimetre galaxies. Building upon previous *Spitzer*-based studies of star formation rate (SFR) evolution (e.g. Pérez-González et al. 2008), the large *Herschel* sample size of Elbaz et al. (2011) allowed the identification of an IR 'main sequence', including local, normal star-forming spirals. In contrast, luminous star-forming galaxies lie above this sequence in a seemingly distinct 'starburst' phase. We have now begun quantifying and characterizing the physical origin of this relationship (e.g. Rodighiero et al. 2014; Speagle et al. 2014; Béthermin et al. 2015; Schreiber et al. 2015).

Herschel blank fields have yielded a large sample of galaxies at $z < 1$, while also glimpsing a few of the brightest star-forming galaxies at higher redshift (e.g. Swinbank et al. 2012; Walter et al. 2012; Riechers et al. 2013). However, observations suffer from the intrinsic limit imposed by instrumental confusion noise (Nguyen et al. 2010), effectively restricting them to galaxies brighter than a demi-ULIRG ($L_{\rm IR} > 5 \times 10^{11}$ L$_\odot$) at $z \gtrsim 1.5$, and ULIRGs beyond $z \sim 2$.

Gravitational lensing by massive galaxy clusters can be of great benefit in the FIR (Smail, Ivison & Blain 1997), boosting background sources out of the confusion noise. There is an added advantage that foreground cluster galaxies are nearly transparent, contributing only a small fraction to the total observed flux. The *Herschel* Lensing Survey (HLS; Egami et al. 2010; in preparation) was the largest *Herschel* programme dedicated to exploiting cluster lensing. The survey design was ably demonstrated by the early observation of the well-known $z = 2.8$ lensed LIRG behind the Bullet cluster (Rex et al. 2010). Accounting for the magnification factor $\mu \sim 75$, the intrinsic flux of the source at 250 μm is <1 mJy, significantly fainter than the nominal confusion limit of SPIRE ($5\sigma \sim 28$ mJy; Nguyen et al. 2010). For a sample of HLS lensed sources, Sklias et al. (2014) explored multiwavelength characteristics, concentrating on optical extinction and star formation histories, while Dessauges-Zavadsky et al. (2015) investigated their molecular gas content and found evidence for a non-universal dust-to-gas ratio. Combes et al. (2012) and Rawle et al. (2014b) highlighted another facet of gravitational lensing, as the magnification and conservation of surface brightness enabled observation of an HLS-discovered source at $z = 5.2$ with sub-kpc resolution millimetre interferometry.

While the lensed, high-redshift galaxies are the primary interest of the HFF programme, many cluster members are also in the observations. Generally, cluster galaxies are quiescent, with little or no dust to produce FIR emission. However, several *Herschel* studies have each detected 10s of cluster members at intermediate redshift (Pereira et al. 2010; Rawle et al. 2010; Coppin et al. 2011; Rawle et al. 2012a,b). Recently, Rawle et al. (2014a) analysed the HFF cluster A2744, demonstrating that IR SFRs and optical morphologies can discriminate cluster formation processes such as group in-fall and cluster merging.

In this paper, we primarily provide a robust flux catalogue of all *Herschel*-detected sources within the HFFs. We also present a 'value-added' catalogue of optical counterparts on a best-effort basis, enabling the calculation of redshift-dependent and intrinsic physical properties such as magnification, IR luminosity and dust temperature. The observations are detailed in Section 2, while Section 3 describes the compilation of the *Herschel* flux catalogue,

Table 2. *Herschel* programmes and observation IDs (OBSIDs) for the Frontier Fields.

Cluster	Programme		PACS OBSIDs	SPIRE OBSIDs
A2744	HLS	KPOT_eegami_1	1342188251–2 ($n = 2$)	1342188584
A370	PEP	KPGT_dlutz_1	1342223332–3 ($n = 2$)	–
	HerMES	KPGT_soliver_1	–	1342201311–8, 1342248002–4 ($n = 11$)
M0416	HLS	OT2_eegami_5	1342250291–2 ($n = 2$)	1342241122
M0717	HLS	KPOT_eegami_1	1342219416–7 ($n = 2$)	1342193012
M1149	HLS	KPOT_eegami_1	1342211797–8 ($n = 2$)	1342222841
	GT	GT1_dlutz_4	1342221954–7 ($n = 4$)	1342210511
AS1063	HLS	KPOT_eegami_1	1342188222–3 ($n = 2$)	1342188165
	HLS	OT2_trawle_3	1342270947–8 ($n = 2$)	–

including photometric extraction and band-merging methodology. Section 4 explains the 'value-added' catalogue, and derives intrinsic star formation properties. Section 5 presents an initial exploration of some of the most interesting IR-bright sources in HFF. Section 6 summarizes the paper. We assume a standard cosmology with $H_0 = 70\,\mathrm{km\,s^{-1}\,Mpc^{-1}}$, $\Omega_\mathrm{M} = 0.3$, $\Omega_\Lambda = 0.7$.

Herschel imaging, catalogues and source IR SEDs associated with this paper can be downloaded from the public flavour of the Rainbow Database.[2]

2 OBSERVATIONS AND DATA REDUCTION

This section describes IR and ancillary data for the HFFs. Each cluster is observed in two distinct regions, referred to as the central and parallel footprints. The data availability for each footprint at the time of writing is summarized in Table 1.

2.1 *Herschel*

The *Herschel Space Observatory* included two broad-band imagers, PACS (Poglitsch et al. 2010) and SPIRE (Griffin et al. 2010). They probed $\lambda \sim 70$–$500\,\mu\mathrm{m}$, which brackets the peak of the IR dust component out to $z \sim 4$. The central HFF footprints were observed by both instruments, while parallel fields are covered by SPIRE only. Here we describe the programmatic origin, observing set-up and reduction for the *Herschel* data, as summarized in Table 2.

2.1.1 PACS

The PACS instrument allowed an observer to choose between 70 or 100 μm bands in a blue channel, collected simultaneously with the red channel at 160 μm. For all six central Frontier Fields footprints, imaging is available within the PACS 100 and 160 μm bands. In addition, M1149 and AS1063 were also covered at 70 μm.

Five clusters were observed by PACS as part of the HLS (Egami et al. 2010; in preparation), which combines an Open-Time Key Programme (KPOT) and an Open-Time Cycle 2 (OT2) Programme (both PI: E. Egami). These (100, 160 μm) observations consist of two orthogonal scan maps, each comprising 18 repetitions of 13 parallel 4-arcmin scan legs (total observing time per cluster, $t_\mathrm{obs} = 4.4$ h). The sixth Frontier Field (A370) was part of the PACS Evolutionary Probe (PEP; Lutz et al. 2011) Guaranteed-Time Key Programme (KPGT). The PEP cluster observing strategy was almost identical to HLS, but with 22 repetitions per orthogonal scan map ($t_\mathrm{obs} = 5.2$ h).

[2] https://rainbowx.fis.ucm.es (Pérez-González et al. 2008)

A GT Cycle 1 (GT1) Programme re-observed M1149 in all three PACS bands (PI: D. Lutz), consisting of two cross-scans per blue band (70 and 100 μm; each $t_\mathrm{obs} = 0.9$ h), comprising three repetitions of 20 parallel 3-arcmin scan legs in a point source map. This also gave 1.8 h of additional depth at 160 μm, concentric with the HLS observation, but over a smaller area.

An ancillary HLS OT2 Programme re-targeted AS1063 to gain 70 μm (PI: T. Rawle). The programme added a further two cross-scans with 27 repetitions each (4-arcmin scan legs), at 70 and 160 μm ($t_\mathrm{obs} = 6.4$ h). This data is coincident with the HLS observations.

Finally, A2744 is located on the edge of the South Galactic Plane coverage of the wide-field PACS observations from H–ATLAS (PI: S. Eales; Eales et al. 2010). The survey was completed in parallel (PACS+SPIRE) mode and achieved a 5σ depth at 100 μm of ∼120 mJy (Ibar et al. 2010). As this is very shallow compared to HLS we do not include the data in our co-added map (hence it is ignored in Table 2). The H–ATLAS PACS data for the A2744 parallel field (not covered by HLS), contain no detections.

Regardless of origin, all PACS data were reduced homogeneously. Calibrated time-stream data (level one frames) were taken directly from the *Herschel* archive and processed by UNIHIPE to produce fits files in the format required by UNIMAP (Piazzo et al. 2012, 2015). UNIMAP employs a Generalized Least Squares (GLS) method to produce the final maps (combining all OBSIDS), and includes a second timeline deglitcher, detection and correction for detector signal jumps, and an advanced drift removal via an Alternate Least Square method. This algorithm has several advantages compared to the naive map-maker PHOTPROJECT (the erstwhile standard for archive products), as it removes the need to filter 1/f noise drift in the PACS bolometers: (1) variations in background flux are conserved rather than smoothed; (2) source fluxes are not truncated, removing the need to mask known sources and allowing blind PSF-fit photometry without using correction functions; (3) all turnaround data can be used, including those observed at zero scan speed, which increases the depth at the edge of the map.

The final PACS images extend to a radius of ∼4–5 arcmin from each cluster core. Generally this only covers the central HFF footprint, although three galaxies on the inner edge of the parallel fields are also just within the PACS maps. The beam sizes have FWHM = 5.2, 7.7 and 12 arcsec at 70, 100 and 160 μm, respectively. The sensitivity of our prior-based flux catalogues (see Section 3.2) at the centre of the PACS maps are given in Table 3.

2.1.2 SPIRE

SPIRE operated at 250, 350 and 500 μm simultaneously, and achieved confusion-limited depth in a very short time. Four HFF clusters were part of the HLS OTKP programme, consisting of 20

Table 3. Median 5σ depth (in mJy) of the prior-based *Herschel* catalogues within the central HFF footprints.

Cluster	PACS 70	PACS 100	PACS 160	SPIRE 250	SPIRE 350	SPIRE 500
A2744	–	4.5	8.8	13.9	14.9	13.0
A370	–	4.1	8.3	13.9	17.2	14.0
M0416	–	4.3	8.0	17.5	14.6	15.5
M0717	–	4.5	8.5	18.6	17.9	17.7
M1149	7.3	4.5	8.6	14.9	15.2	17.8
AS1063	3.1	4.7	8.2	16.2	17.1	17.5

repetitions in large scan map mode, each with two 4-arcmin scans and cross-scans (per cluster, $t_{\rm obs} = 1.7$ h). SPIRE coverage of M0416 is from HLS OT2, and was achieved via a 10-repetition small scan map (1 scan and one cross-scan of 4 arcmin length; $t_{\rm obs} = 0.4$ h). The resulting map is a little smaller and shallower than the original HLS observations. A370 was included in the KPGT Herschel Multi-tiered Extragalactic Survey (HerMES; Oliver et al. 2012), and the data combines eight small scan maps (six repetitions each) and three large scan maps (one repetition, seven scans and seven cross-scans of 38 arcmin length). The overall SPIRE observing time for A370 was $t_{\rm obs} = 3.5$ h, but due to the wider footprint this corresponds to a similar central depth as the HLS maps. H–ATLAS parallel mode SPIRE observations (5σ at 250 μm ∼33 mJy; Clements et al. 2010) also cover A2744, but are ignored as the shallow data contribute nothing extra to the confusion-limited HLS.

For all six clusters, images were produced via the standard reduction pipeline in HIPE (Ott 2010) v12 (v12.2 calibration product) with median baseline removal and destriper. Including all turnaround data, the final SPIRE images extend to a cluster centric radius of ∼10 arcmin (HLS OTKP), ∼7 arcmin (M0416) and ∼30 arcmin (A370). In all clusters except M0416, both central and parallel footprints are covered. For M0416, one third of the parallel field falls outside of the SPIRE image. The beam sizes are large (18, 25, 36 arcsec, respectively) and all three bands are confusion limited ($5\sigma_{\rm conf} \approx 28, 32, 33$ mJy; Nguyen et al. 2010). However, this confusion limit assumes that the local source density is unknown, but with a prior knowledge of source distribution from shorter wavelength data (see Section 3.2), we reach a significantly lower flux limit in the central fields (see Table 3).

2.2 Infrared ancillary data

The prior-based photometry method described in Section 3.2 depends heavily on observations from the *Spitzer Space Telescope*. The IR SED fitting procedures in Section 4.4 use all available IR photometry $\lambda \gtrsim 3$ μm. Here we briefly describe IR imaging that originates from facilities other than *Herschel*.

2.2.1 *Spitzer*

Spitzer data for HFF were extracted from the *Spitzer* Heritage archive.[3] For IRAC, we started from the reduced, flux-and-WCS calibrated images provided in the archive as 'corrected Basic Calibrated Data' (cBCD) and mosaic them together using the procedure developed by Huang et al. (2004). This procedure includes pointing refinement, distortion correction, drizzling to a scale half of the original (∼0.6 arcsec pixel^{-1}) and correction of detector artefacts (most noticeably, mux-bleeding). In the case of MIPS, we started from the post-BCD products downloaded from the archive and used MOPEX v1.8 for the flat fielding, jailbar removal and mosaicking. We used a pixel scale of 1.2 arcsec pixel^{-1}.

All six cluster centres are covered by imaging in the 3.6 and 4.5 μm IRAC bands (beam size of 1.7 arcsec), with median 5σ sensitivities of ∼1.7 and ∼1.6 μJy, respectively. Four clusters are also observed using the IRAC 5.8 and 8 μm channels (beam size of 1.7, 1.9 arcsec), yielding a median 5σ depth of ∼5.2 μJy, and by MIPS 24 μm (6 arcsec beam diameter) with a median 5σ sensitivity of ∼90 μJy. The parallel fields unfortunately have a less uniform *Spitzer* coverage, with the details described in Table 1.

The heterogeneity results in no attempt by this study to derive stellar masses from the NIR. We defer this aspect to future analyses, which will be able to employ the deeper, homogeneous IRAC observations currently underway.

2.2.2 *WISE*

The four-band, all-sky *WISE* mission covers 3.4, 4.6, 12, 22 μm (Wright et al. 2010). Imaging and catalogues for all of the HFF footprints were obtained from the NASA/IPAC Infrared Science Archive (IRSA).[4] Sensitivity in each band varies across the sky, but is typically 0.25, 0.35, 3.0, 18.0 mJy (5σ), with beam sizes 6.1, 6.4, 6.5, 12 arcsec (PSF FWHM). Source blending within the 12 arcsec beam at 22 μm is a major issue, and we generally disregard fluxes in this band for SED fitting.

2.3 Counterpart ancillary data

Knowledge of the source redshift is a pre-requisite for the derivation of magnification and intrinsic physical properties from IR SEDs. Redshifts are generally obtained from optical data, so we identify a candidate optical counterpart for each IR source on a best-effort basis (Section 4). Here we briefly describe the imaging and spectroscopy relevant to that process.

2.3.1 *HST imaging*

The fully completed HFFs programme will comprise seven-band observations from ACS (*F*435*W*, *F*606*W* and *F*814*W*) and WFC3 (*F*105*W*, *F*125*W*, *F*140*W*, *F*160*W*). The wider field ACS images (∼3.4 × 3.4 arcmin) define our area of interest. Smaller (∼2.0 × 2.3 arcmin) WFC3 footprints are concentric with the ACS coverage, and are useful for probing the redder sources often associated with *Herschel* flux.

At the time of writing, HFF observations for A2744, M0416 and M0717 are complete, while M1149, A370 and AS1063 are due to be concluded by Cycle 22 (2015–16). For counterpart identification, we use the best available *HST* imaging taken directly from the Hubble Legacy Archive.[5] We defer to a future paper *HST*-derived homogeneous photometric redshifts, stellar masses and morphologies, as this will be possible only when the full HFF observing programme is complete. Section 2.3.4 details the heterogeneous photometric redshifts that we do employ in this study.

[3] http://irsa.ipac.caltech.edu/applications/Spitzer/SHA

[4] http://irsa.ipac.caltech.edu/Missions/wise.html

[5] http://hla.stsci.edu/

2.3.2 VLA

A useful stepping stone in counterpart identification is broad-band radio interferometry, which probes the same star formation dominated sources as *Herschel* with arcsec-scale spatial resolution.

M0416, M0717 and M1149, are covered by public Jansky VLA 3 GHz (∼10 cm) imaging data (programme ID: VLA/13B-038, PI: M. Aravena). The resulting maps easily cover HFF central and parallel footprints, with restored beam sizes (FWHM) of 2.5 × 1.9, 1.8 × 1.0 and 1.8 × 1.0 arcsec respectively and a 5σ sensitivity limit of ∼6 μJy beam^{-1}. For A370, we use the VLA 1.4 GHz (∼21 cm) source catalogue presented in Wold et al. (2012), which covers both HFF footprints within a 40 × 40 arcmin field. The map has a synthesized beam of 1.8 × 1.6 arcsec, and a 5σ noise of ∼30 μJy beam^{-1} for the HFF centre.

2.3.3 Spectroscopy

Many of the spectroscopic redshifts used within this study are from large public compilations: Owers et al. (2011) for A2744 (11 redshifts), Wold et al. (2012) for A370 (12), Ebeling, Ma & Barrett (2014) for M0416, M0717 and M1149 (23 in total) and Gómez et al. (2012) for AS1063 (7). Several further publications provide individual redshifts, as noted in the catalogue tables.

We also present 33 previously unpublished redshifts:

2.3.3.1 HST grism

Our catalogue includes 19 spectroscopic redshifts from our own reduction of the publicly available *HST* data of the Grism Lens-Amplified Survey from Space (GLASS; Schmidt et al. 2014; Wang et al. 2015), covering the central ∼2 × 2 arcmin of each cluster. The *HST* grism data were reduced using AXE (Kümmel et al. 2009), and multiple visits were drizzled together using MULTIDRIZZLE, with the routine TWEAKSHIFTS determining offsets.

2.3.3.2 LBT/MODS

Optical spectra for 13 objects in M0717 (two masks) and M1149 (one mask) were obtained using the 6 × 6 arcmin FoV LBT/MODS on 2013 January 19 and 2013 April 8. MODS was used in the grating mode with resolutions of 1850 (blue channel) and 2300 (red), pixel scales 0.120 arcsec pixel^{-1} and 0.123 arcsec pixel^{-1}, and a combined wavelength range of 3200–10 500 Å. The average seeing was between 0.57–0.97 arcsec. Data reduction used MODSCCDRED and MODSIDL,[6] with sky subtraction based on the Kelson (2003) 2D B-splines algorithm, reducing residuals from skylines and minimizing noise in the spectra.

2.3.3.3 Magellan/IMACS

One spectrum is derived from optical observations of A370 obtained using the Magellan/IMACS f/4 camera on 2013 September 5. The 150 lines/mm grating provides a dispersion of 1.453 Å pixel^{-1} and covers a wavelength range of 3650–9740 Å. IMACS f/4 has a 15.4 × 15.4 arcmin FoV with a pixel scale of 0.111 arcmin pixel^{-1}. The average seeing during the observation was 0.68 arcsec. We employed the COSMOS data reduction package (Dressler et al. 2011), which includes sky subtraction based on the Kelson (2003) algorithm.

2.3.4 Photometric redshifts

Four of the Frontier Fields (M0416, M0717, M1149, AS1063) are included in the Cluster Lensing And Supernova Survey with Hubble (CLASH; Postman et al. 2012). Optical counterparts in these clusters without a spectroscopic redshift rely on well-constrained CLASH photometric redshifts, based on 16-band *HST* photometry or 5–8 band 8 m-class ground-based imaging (Umetsu et al. 2014). We direct the reader to the above papers or data archive[7] for further details.

We do not attempt to produce our own optical photometric redshift estimates for the remaining clusters as the complete merging of all optical/NIR ground-based observations will be presented in future papers. However, for counterparts without either a spectroscopic or CLASH photometric redshift, we use an 'IR photometric redshift' estimate, described in Section 4.4.1.

3 MERGED IR FLUX CATALOGUE

In this section we describe the band-merged photometry methodology, culminating in the presentation of our *Herschel* flux catalogue for HFF.

Band-merged catalogues in the wavelength range covered by *WISE*, *Spitzer* and *Herschel* were produced within the Rainbow Cosmological Surveys Database framework (Pérez-González et al. 2008). Photometric extraction follows the method described in Pérez-González et al. (2010). The same procedure was followed for each cluster.

3.1 Image alignment

Herschel maps were aligned to *Spitzer* astrometry using a global *x*–*y* offset based on a stack of the brightest few tens of *Herschel* point sources. In reality, the offset was only calculated for PACS 100 and SPIRE 250 μm, as the well-known *Herschel* optical models ensure that offsets between bands of the same instrument are well calibrated. Hence we applied the same offset for both PACS bands and a second one for all three SPIRE bands. At 500 μm, this assumption is crucial, as the large beam size and small number of sources within the *Spitzer*-observed regions render a direct offset characterization very uncertain. Generally, the offsets required to align pipeline *Herschel* images to the *Spitzer* astrometry are small, with a mean of 1.1 and 1.6 arcsec for PACS and SPIRE respectively (cf. FWHM >5 arcsec).

We also tested the application of a more elaborate transformation to the *Herschel* imaging, including stretch and rotation as well as offset. However, the final maps were negligibly different, the degree of freedom was worryingly high for the number of available reference points, and the band-to-band transferal of the transformation was significantly more complicated. Therefore we decided to adopt the simpler *x*–*y*-offset transform.

3.2 Multiband photometry

Photometric extraction in the *Herschel* bands rely on prior catalogues from the bluer, and higher-spatial resolution, *Spitzer* IRAC

[6] http://www.astronomy.ohio-state.edu/MODS/Software

[7] https://archive.stsci.edu/prepds/clash/

and MIPS imaging. Therefore, we begun by creating 3σ direct-detection catalogues for each *Spitzer* band in turn, using an iterative aperture photometry technique. Each pair of *Spitzer* catalogues were merged via a simple counterpart algorithm, using a maximum search radius of the largest PSF FWHM in the pair, to produce a master IRAC/MIPS catalogue. The IRSA *WISE* catalogue was trivially linked to the IRAC/MIPS catalogue by finding the nearest IRAC–*WISE* source pairs.

Photometry for each *Herschel* image used a simultaneous PSF-fitting algorithm, allocating FIR flux in each band to shorter wavelength priors. While this method is very good at de-blending close, but ultimately resolved complexes of *Herschel* flux, the large number of priors from deep IRAC imaging runs the risk of incorrectly de-blending *Herschel* point sources into several constituent parts. To avoid the latter, we replaced close (sub-*Herschel* PSF FWHM) groups of *Spitzer* sources with a single 'pseudo-source', corresponding to the position of the brightest source in that group. For each group, the number ('multiplicity') and identity of all sources is propagated through the scripts. The choice of position for a pseudo source is ultimately not significant, as we also allowed small offsets within the simultaneous PSF fitting mechanism. Furthermore, although we start with the location of the brightest grouped source for the prior-based fit, that does not influence which IRAC source we ultimately select as the counterpart (see below, and Section 4).

We began with PACS 100 μm, as the band with the best combination of spatial resolution, sensitivity and coverage for all clusters. We adapted the *Spitzer* prior catalogue by grouping sources within 5 arcsec diameters of each other and then proceeded with the simultaneous PSF fitting, allowing for small offsets necessary due to the effect of different pixel sizes. Fluxes were derived via aperture photometry on the fitted PSF, allowing us to use the same aperture and corrections as for a direct detection. The resulting catalogue automatically includes prior information for each PACS source, and where a 'pseudo-source' is allocated PACS flux, all potential counterparts are recorded. For sources detected by PACS but too faint for, or beyond the coverage of, *Spitzer*, we also produced a list of direct detections based on the residual image, ie the remaining 100 μm sources after all the fitted flux has been removed. Flux was measured using aperture photometry and the direct detections were added to the PACS 100 μm photometry catalogue and flagged.

The full procedure was then repeated for 70 and 160 μm, using the PSF FWHM to define the *Spitzer* prior catalogue grouping diameter. After completing the simultaneous fitting and direct-detection stages, we merged the independent PACS catalogues. First we matched common IRAC/MIPS priors and psuedo-sources, and then used a search radius of 4 arcsec to match the remainder. For PACS sources undetected in one or two other PACS band, we force photometric measurement in the residual images.

For the SPIRE bands, the same iterative procedure was applied, varying the prior catalogue grouping scale to correspond with the SPIRE PSF FWHM. The only other difference is the inclusion of the direct-detection PACS sources in the prior catalogue (in effect a merged *Spitzer*/PACS prior list). Once a catalogue was produced for each of the three SPIRE bands independently (including the direct-detection step on the residual maps), we proceeded with the SPIRE-band merging, following the example of the PACS bands, with forced photometry in the cases of single-band non-detections.

The prior-based methodology helps to de-blend confused *Herschel* sources, and ensures a straight-forward combination of the inter-connected IRAC, *WISE*, MIPS, PACS and SPIRE catalogues. Furthermore, multiple possible priors from the grouping procedure can often be reduced to a single dominant prior by accounting for the location of intermediary MIPS or PACS flux and/or the inferred SED. For example, most SPIRE sources have a single PACS counterpart, which in turn corresponds to a single MIPS source, which itself has one plausible IRAC counterpart (based on flux or SED shape). So although several IRAC sources may have been included within the grouping for a SPIRE source, the intermediate bands suggest a unique counterpart.

3.3 HFF *Herschel* flux catalogue

Our primary goal is to create a *Herschel* catalogue within the HFF footprints, so every source beyond the ACS image boundaries[8] is ignored.

The only other selection criterion concerns the definition of '*Herschel*-detected': any source having at least two $>4\sigma$-significance *Herschel* fluxes, regardless of filter or detection by any of the ancillary facilities. We stress that by simultaneously fitting to priors, we will account for and remove fainter ($<4\sigma$) *Herschel* source flux from the fluxes of brighter galaxies, even if they themselves are not included in the final catalogue. However, we caution that we may be bias against the faintest, reddest IR sources which exhibit a dust continuum peak at SPIRE 500 μm or beyond and are extremely faint in bluer *Herschel* bands.

The final catalogue contains 263 *Herschel*-detected sources, 187 within the central regions and a further 76 within the parallel footprints. The difference in source density (the two footprints have equal area) can be trivially linked to the lack of *Spitzer* and PACS coverage for large parts of the parallel fields, meaning that detection of a *Herschel* source relies on SPIRE alone. Figs 1 and 2 identify the sources in PACS (for central footprints) and SPIRE (for both footprints). *Herschel* fluxes are presented in Table 4.

There are 230/263 catalogue sources with a *Spitzer* counterpart and 131/263 detected by *WISE* (112 overlap). Of the *Spitzer* sources, 146/230 have both PACS and SPIRE detections, while 36 are only detected in PACS and 48 by SPIRE alone. The mean grouping 'multiplicity' of the priors for the PACS sources is ∼1.3, which indicates that matching PACS to IRAC is relative trivial. For the SPIRE sources this mean multiplicity rises to ∼3.4.

The 33/263 sources without a *Spitzer* counterpart are almost exclusively located beyond the available IRAC and MIPS coverage, and are direct detections in either PACS or SPIRE. Only two were direct detections in PACS, and both are also detected by SPIRE. One of those (HLSJ001401.3–302224 in A2744) lies just beyond the *Spitzer* imaging and just inside the PACS coverage, but is well detected by *WISE*. The other (HLSJ041606.6–240528 in M0416) is located within the core of the cluster, in a region densely populated and extremely blended in IRAC (and also in *WISE*). This is the only case for which we were unable to extract IRAC photometry for a *Herschel* source within the IRAC image bounds. Unfortunately, MIPS is unavailable for M0416.

The remaining 31 sources are SPIRE direct detections in the parallel fields beyond current IRAC, MIPS or PACS coverage. 18/31 are detected by *WISE*. Therefore, only 14/263 *Herschel* sources (1 PACS + 13 SPIRE) lack NIR counterparts and SED information between 1 and 70 μm. Pre-empting the next section, it is worth noting here that despite the lack of *Spitzer* or *WISE* data, two of these 14 sources have VLA (and hence secure *HST*) counterparts, and a further five have unambiguous *HST* associations.

[8] http://www.stsci.edu/hst/campaigns/frontier-fields/HST-Survey

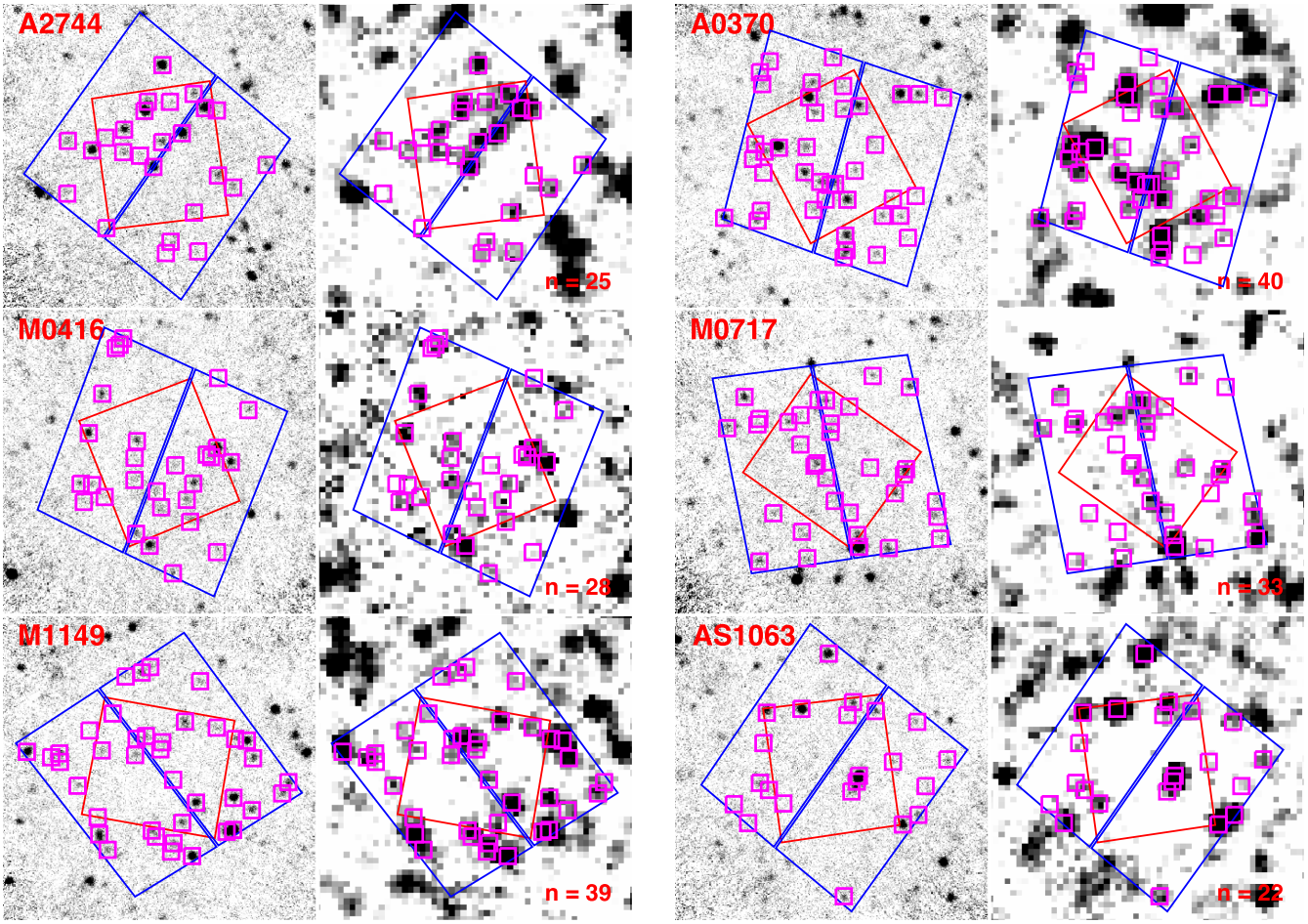

Figure 1. *Herschel* imaging for the HFF central regions: PACS 100 μm (left of pair) and SPIRE 250 μm (right of pair). HFF footprints are marked in red (WFC3) and blue (ACS). *Herschel*-detected sources are highlighted by magenta squares.

4 COUNTERPART ANALYSIS

Analysis of the intrinsic properties (e.g. IR luminosity, dust temperature) of *Herschel* sources relies on a knowledge of the redshift. This is particularly true for background objects, as the magnification factor (μ) is also a function of redshift behind the lensing mass.

We therefore attempt to provide a best-effort 'value-added' catalogue for the sources detected by *Herschel*, identifying the most likely optical counterpart, which in turn leads to redshift information.

4.1 Counterpart identification

For each IR source we locate the best optical counterpart using a variety of techniques and all available data. The first-guess counterpart for many *Herschel* sources was the *HST* object at the position of the prior-based IRAC source. For the three clusters with complete HFF *HST* images (A2744, M0416 and M0717), Figs 3–5 highlight that there is an obvious optical counterpart for many of the *Herschel*-detected sources. We verify these by ensuring that the IR SED (i.e. dust peak and temperature) is reasonable when assuming that the IR source is at the optical redshift. We similarly eliminate other nearby optical sources as potential candidates.

Previous work on optical–FIR source matching has employed a similar approach to our PSF fitting (e.g. Hwang et al. 2010; Elbaz et al. 2011; Domínguez Sánchez et al. 2014; Pappalardo et al. 2015). Working with the larger GOODS catalogues, Elbaz et al. (2011) kept only fluxes that were considered reliable by a 'clean index', somewhat similar to our 'multiplicity' in that it encapsulates the number of prior sources within the *Herschel* PSF FWHM. However, the small size of the HFF sample allowed us to individually examine each source, and find the best candidate counterpart for each. This is particularly important for sources in which the shortest wavelength (i.e. highest resolution) *Hershel* flux originated from a 'grouped' *Spitzer* counterpart; we do not want to just use the brightest IRAC source. Instead, we consult the imaging and SED to choose the best-fitting counterpart, as described in Section 3.2. When multiple potential counterparts are at a similar on-sky position but different redshift, the shape of the IR continuum (discussed in Section 4.4) can be used as an effective discriminator.

Furthermore, we do not just use the IR SED and *HST* imaging to identify the candidate counterpart. As mentioned in Section 2.3.2, high spatial resolution radio observations offer a valuable additional constraint on the origin of the IR emission, often allowing us to pinpoint the responsible *HST* counterpart or even sub-component (Geach et al. 2015; Thomson et al. 2015). 91 *Herschel* sources have an associated radio detection, from 187/263 located within available VLA maps. We use these to successfully validate our chosen *HST*/IRAC counterpart, and find very few mismatches. We estimate that of the remaining 172 *Herschel*-detected sources, the counterpart of <5 per cent would change given additional VLA observations (such as the upcoming HFF

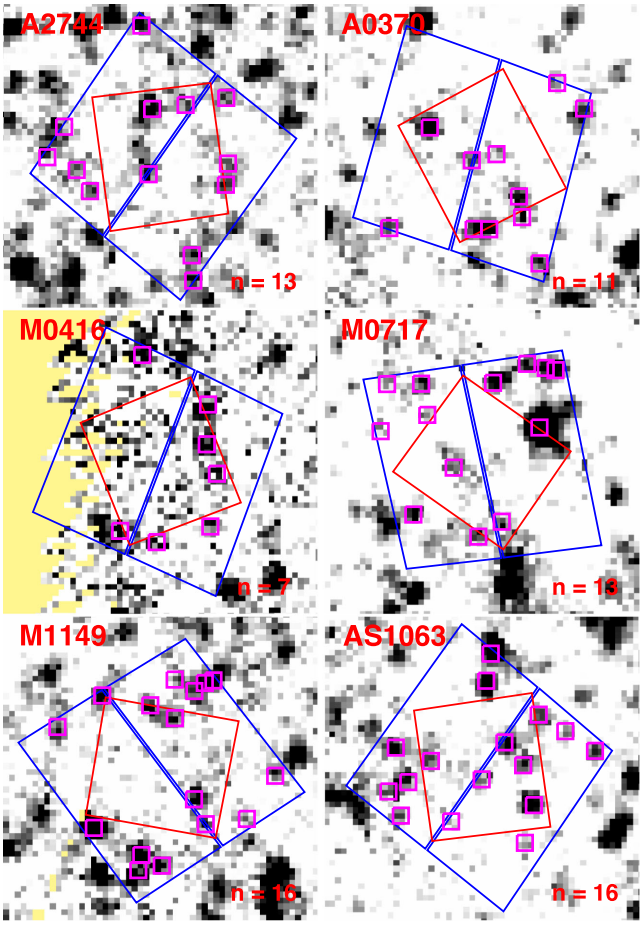

Figure 2. Herschel SPIRE 250 μm imaging for the HFF parallel fields (markings as in Fig. 1). Regions beyond the SPIRE coverage are shaded yellow.

programme, PI: Murphy). Such future refinements will be applied to the online version of our 'value-added' *Herschel* catalogue as required.

We emphasize here the prior-based source extraction, 'by-eye' multiwavelength counterpart matching (including radio data) and optical–IR SED fitting were not executed sequentially or in isolation. The best counterpart for each individual *Herschel* source was selected based on all of the available information simultaneously.

4.2 Counterpart redshift

In this paper, the counterparts are primarily used to yield a source redshift. More than 40 per cent (112/263) have spectroscopic redshifts, taken from various studies (as described in Section 2.3.3). A further 89 have well-constrained photometric redshift estimates from the multiband CLASH catalogues (see Section 2.3.4). The remaining 62 sources have a redshift estimated from the best-fitting IR SED templates, which is described further in Section 4.4.1. This will be updated in the online 'value-added' catalogue as spectroscopic surveys target further *Herschel* counterparts. Table 5 provides a full breakdown of the number of sources with each type of redshift, while Figs 3–5 also indicate their origin. We discuss the distribution of redshifts in Section 5.1.

4.3 Magnification factors

Sources within the foreground or associated with the cluster itself (typically taken as $z < z_{\rm cl} + 0.1$) are assumed to have a zero magnification.

Recent years have seen a huge effort to constrain lensing models for the Frontier Fields. Within the central areas, we employ the CATS models (Jauzac et al. 2012, 2014; Richard et al. 2014) derived using the publicly available LENSTOOL package (Jullo & Kneib 2009). Within CATS, the cluster mass is represented by a combination of two types of component: (1) known cluster galaxies, with spectroscopically confirmed redshifts and masses scaled from their luminosity, (2) one or more large-scale, smooth haloes. The models were refined by comparing predictions to the known sets of well-constrained multiple images in each cluster. The CATS lens models cover a 5.3 × 6.1 arcmin area.

We compare the CATS-derived magnifications with those from the 'light-traces-mass' models based on the method of Zitrin et al. (2009). We find a good agreement between Zitrin and CATS, with a median difference in the magnification factor of $\Delta\mu \sim 0.1$ (rms dispersion ∼0.5).

In the parallel fields, we are forced to use the low-resolution, wide-field initial solution from SAWLENS (Merten et al. 2009, 2011), which is a non-parametric model based on strong and weak lensing. In the central regions, where a direct comparison is possible, CATS and SAWLENS also agree well, with a median difference in magnification for our sources of $\Delta\mu < 0.1$. In the outer regions, magnification factors are generally less well-constrained, but are also typically small ($\mu \approx 1$).

Table 4. Observed PACS and SPIRE fluxes for *Herschel*-detected sources within the HFFs.

ID (ref)[a]	Field[b]	S_{70} (mJy)	S_{100} (mJy)	S_{160} (mJy)	S_{250} (mJy)	S_{350} (mJy)	S_{500} (mJy)
HLSJ001412.7–302359 (P)	A2744 C	–	5.2 ± 0.9	10.5 ± 1.8	13.1 ± 2.9	6.8 ± 3.0	–
HLSJ001415.3–302423 (P)	A2744 C	–	5.6 ± 0.8	10.2 ± 2.1	14.8 ± 2.8	–	–
HLSJ001416.7–302304 (P)	A2744 C	–	2.5 ± 0.6	7.5 ± 1.3	–	–	–
HLSJ001416.5–302410 (P)	A2744 C	–	7.2 ± 0.9	11.8 ± 1.6	9.8 ± 5.5	8.4 ± 5.9	6.3 ± 9.2
HLSJ001418.5–302246 (P)	A2744 C	–	7.6 ± 0.9	12.4 ± 1.6	12.6 ± 3.3	6.3 ± 2.8	–
HLSJ001417.6–302301 (P)	A2744 C	–	25.5 ± 2.1	62.4 ± 5.1	66.1 ± 5.2	47.5 ± 4.8	21.5 ± 4.8
HLSJ001418.5–302448 (P)	A2744 C	–	4.5 ± 0.9	11.9 ± 1.6	18.5 ± 2.6	14.2 ± 2.9	8.1 ± 2.6
HLSJ001418.0–302529 (S)	A2744 C	–	–	–	7.7 ± 2.3	12.1 ± 3.4	14.2 ± 3.3
...	...	...	...	...	...	...	...

Notes. The full table is published in the electronic version of the paper. A portion is shown here for illustration.
[a] *Herschel* ID derived from PACS (P) or SPIRE (S) catalogue position.
[b] C=central region; P=parallel.

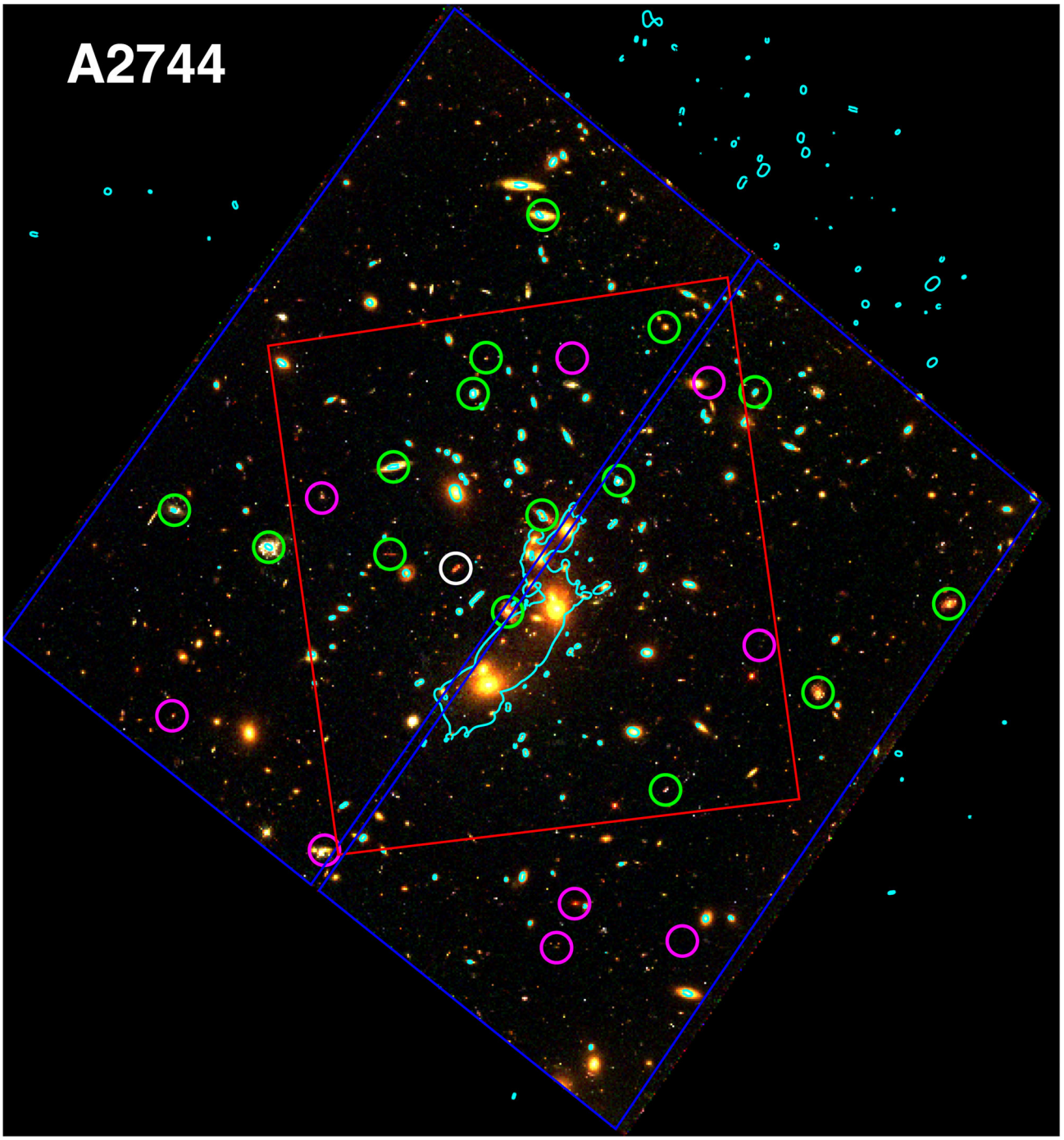

Figure 3. *HST* three-colour image of the A2744 central field, with footprints as in Fig. 1 and lensing critical lines for background sources at $z = 1$ given in cyan (from the CATS models; see Section 4.3). *Herschel*-detected sources are shown by circles (corresponding to the PACS PSF FWHM ∼8 arcsec) and show many counterparts are readily identifiable. Circle colours indicate the origin of the counterpart redshift: green=spectroscopic, white=CLASH optical photometric, magenta=IR-based estimate.

4.4 IR SEDs

Derivation of the physical properties requires an IR model template fit to the dust emission continuum.

Template fitting is executed in the rest-frame, with observed (image plane) fluxes (ie uncorrected for magnification), as presented in the SED figures later in this section. IR properties, however, are given in the source plane: intrinsic values corrected for magnification. We assume that differential (wavelength-dependent) effects are negligible. All uncertainties for output properties are bootstrapped via 1000 Monte Carlo simulations based on the estimated errors in flux, redshift and template-to-template variation.

4.4.1 IR redshift estimate

For all sources, we first estimate an approximate redshift ($z_{\rm phot\_FIR}$) from a modified blackbody with a specific characteristic dust

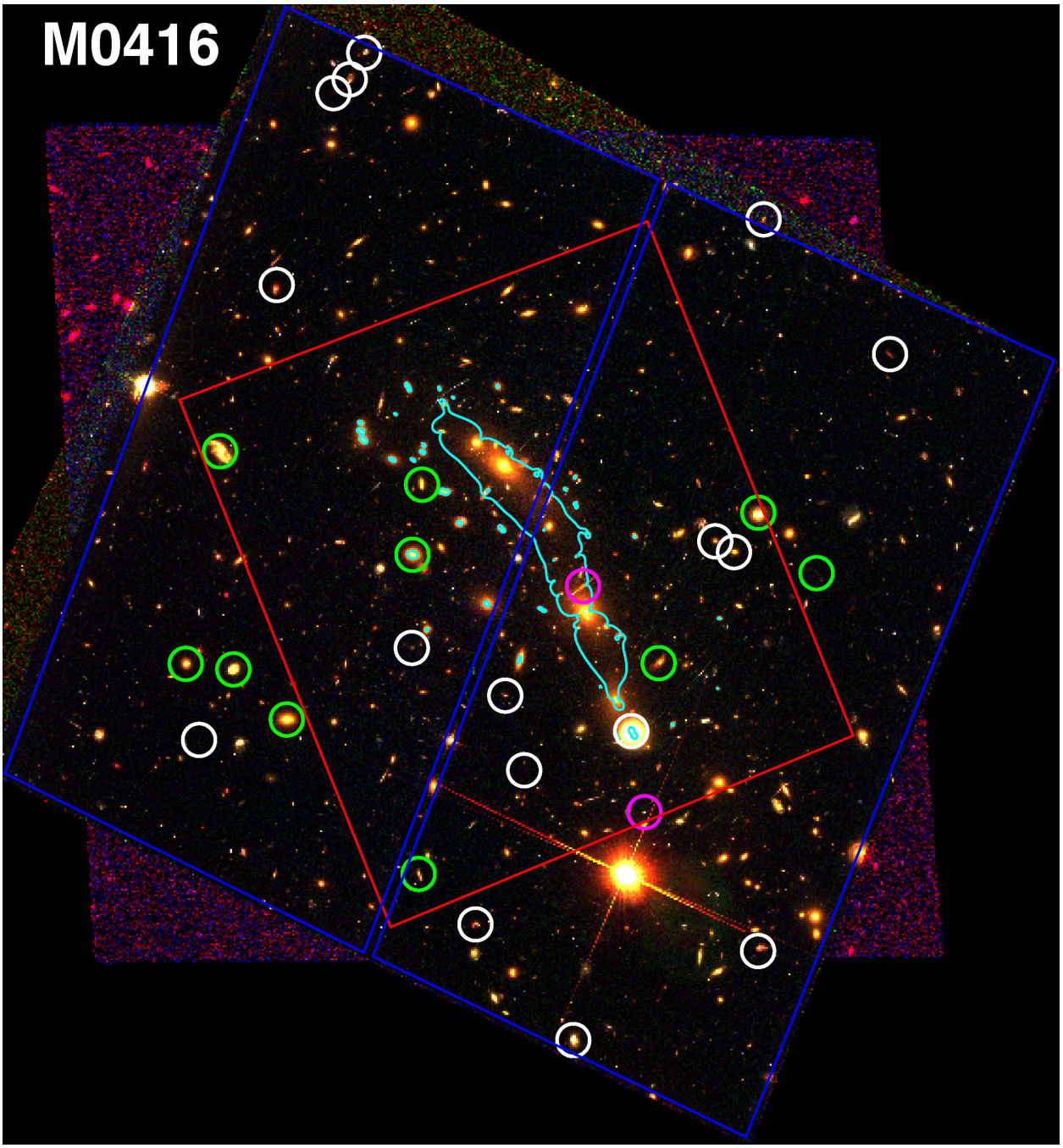

Figure 4. *HST* three-colour image of the M0416 central field. Layout as in Fig. 3.

temperature ($T_{\rm dust}$). Rather than assuming the same temperature in every case, we attempt to soften the temperature–redshift degeneracy using the best-fitting Rieke et al. (2009) template. The technique is possible because the templates exhibit a skewness which varies smoothly with temperature. Hence, the best-fitting skew gives a coarse temperature estimation.

Fig. 6 demonstrates the validity of this method, comparing $z_{\rm phot\_FIR}$ to available spectroscopic (or well-constrained optical photometric) redshifts. For many sources, the FIR-derived redshift is reasonably good, with a mean scatter in the offset of $\sim$0.3, equating to $\delta z_{\rm phot\_FIR}/(1+z_{\rm spec}) \sim 0.40$. This is not dissimilar to the uncertainty estimated by previous attempts at IR-based redshifts, e.g. Pearson et al. (2013). Several of the most obvious outliers result from poor dust peak sampling, which hinders quantification of the skewness. For instance, the two spectroscopic sources with overestimated $z_{\rm phot\_FIR}$ are at low redshift ($z_{\rm best} \sim 0.3$) and are within a parallel field which lacks the PACS coverage to adequately constrain the continuum peak. Their temperature is estimated to be higher than it should, resulting in a correspondingly higher redshift as well.

For the 62 sources without a spectroscopic or well-constrained (CLASH) optical photometric redshift, we use $z_{\rm phot\_FIR}$ when deriving intrinsic properties. We visually inspect the SEDs of all these sources to ensure that the IR continuum templates at the specified

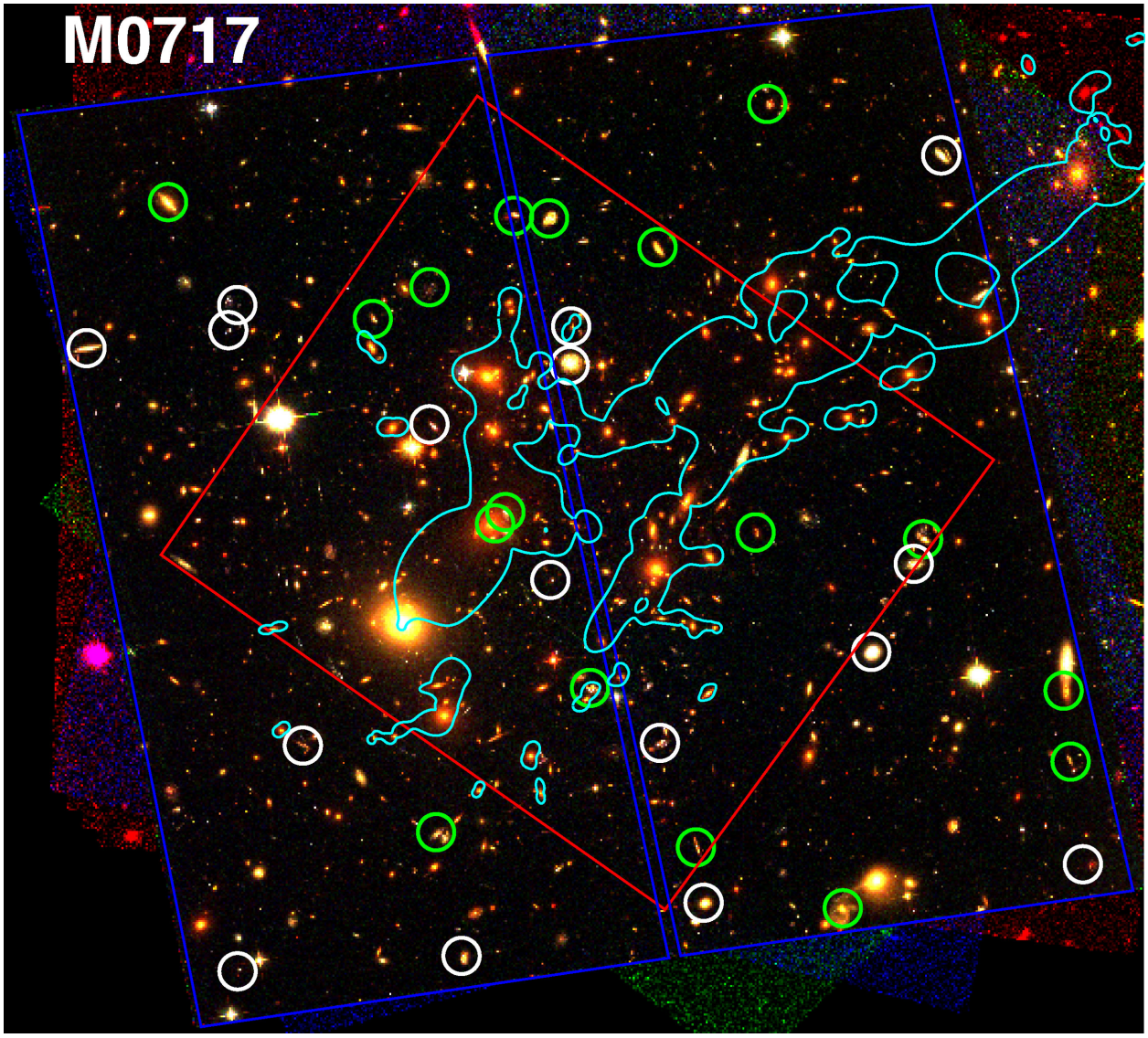

Figure 5. *HST* three-colour image of the M0717 central field. Layout as in Fig. 3.

Table 5. Number of sources within each *HST* footprint, binned by the origin of the counterpart redshift.

Cluster	Central				Parallel				Total
	S[a]	P[b]	IR[c]	Tot	S[a]	P[b]	IR[c]	Tot	
A2744	15	1	9	25	3	0	10	13	38
A370	26	0	14	40	2	0	9	11	51
M0416	10	16	2	28	0	7	0	7	35
M0717	17	16	0	33	3	10	0	13	46
M1149	23	16	0	39	2	14	0	16	55
AS1063	11	9	2	22	0	0	16	16	38
Total	102	58	27	187	10	31	35	76	263

[a]Spectroscopic redshift.
[b]CLASH *HST* or Subaru photometric redshift.
[c]IR SED redshift estimate.

redshift are a close fit to the observed NIR (e.g. IRAC) photometry. For sources outside *Spitzer* coverage (such as the two sources highlighted above), the *WISE* photometry has insufficient precision to discriminate between different redshifts.

Sources for which $z_{\rm best} = z_{\rm phot\_FIR}$ are flagged in our value-added catalogue, and whilst $z_{\rm phot\_FIR}$ appears well behaved, we would still caution against their use for critical applications (such as ALMA spectral set-up).

4.4.2 *Characteristic dust temperature*

The characteristic dust temperature ($T_{\rm dust}$) of the IR component is calculated via the best-fitting single-temperature modified blackbody. Dust heating by the Cosmic Microwave Background is assumed to be negligible, which is reasonable for sources at $z < 4$ (da Cunha et al. 2013). Dust temperature is degenerate with the emissivity index β (e.g. Blain, Barnard & Chapman 2003), and we

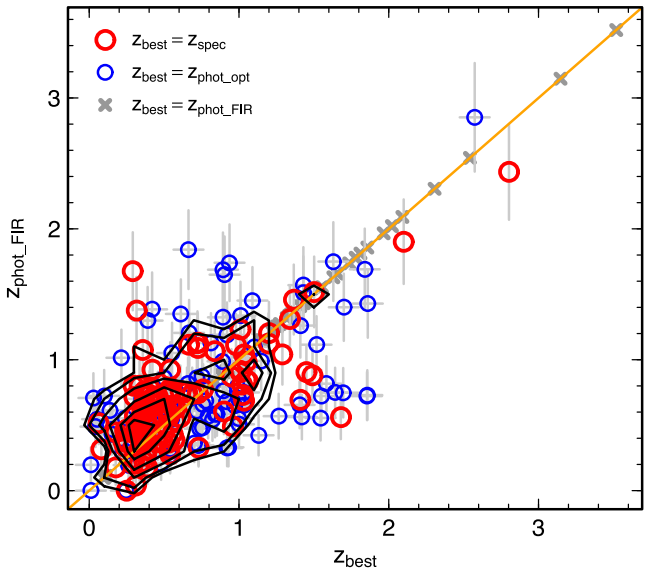

Figure 6. Comparison of the FIR redshift estimate ($z_{\rm phot\_FIR}$) with spectroscopic (large red circles) and optical photometric (small blue circles) counterpart redshifts. Black contours visualize the joint distribution of both these populations. Generally, the FIR estimate is reasonable, showing a scatter of $\Delta z \sim 0.3$. Grey crosses show the 61/263 sources for which we use $z_{\rm best} = z_{\rm phot\_FIR}$. This is solely to show the relative range of redshifts for sources without a good estimate, and they are of course not included in the scatter estimates.

assume $\beta = 2.0$. Using $\beta = 1.5$ would systematically increase $T_{\rm dust}$ by ∼10 per cent.

Dust temperature is also degenerate with redshift, and the two values are inextricably linked for sources with only a $z_{\rm phot\_FIR}$ ($T_{\rm dust}$ is used by the estimation technique). Therefore, for those 62 sources, we simply give the coarse $T_{\rm dust}$ estimate described in Section 4.4.1.

4.4.3 Star formation rate

The total IR luminosity ($L_{\rm IR}$) is derived from the best-fitting Rieke et al. (2009) template to the *Herschel* fluxes, allowing for an overall normalization parameter. Following the standard definition of $L_{\rm IR}$, we integrate over the rest-frame wavelength range $\lambda = 8$–1000 μm. The SFR estimate follows directly via the Kennicutt (1998) relation, modified to match a Kroupa (2002)-like initial mass function as in Rieke et al. (2009).[9] Note that we do not make a correction for unobscured SFR.

For all sources, we also calculate SFR via an identical integration of the best-fitting Berta et al. (2013) template to all available IR photometry. The SED figures throughout this paper show the best-fitting template and derived SFR parameters from both Rieke et al. (2009) and Berta et al. (2013). We find a good agreement between the two derived SFRs: a median discrepancy of 0.08 dex and an rms scatter of 0.18 dex. The uncertainty introduced by the intrinsic shape of the template sets is dominated by the photometric error for all sources, while the redshift uncertainty is also significant for those without a spectroscopic redshift. For simplicity, the catalogues tabulate IR properties derived from the Rieke et al. (2009) templates only.

[9] SFR $[{\rm M}_\odot\ {\rm yr}^{-1}] = 0.66 \times {\rm SFR}_{\rm K98} = 1.14 \times 10^{-10}\ L_{\rm IR}\ [{\rm L}_\odot]$

4.4.4 AGN contamination

A strong active galactic nucleus (AGN) may artificially boost the SFR by contributing flux in the mid-IR. For all SEDs with at least one flux measurement in the 20–200 μm wavelength range, we find the best-fitting sum of a Rieke et al. (2009) template and the mean low-luminosity AGN from Mullaney et al. (2011).

Very few sources (six) have a non-negligible (>10 per cent) contribution to $L_{\rm IR}$ from the AGN component. For those, we calculate $L_{\rm IR}$ and SFR from the star-forming dust component alone (ie integrate only the Rieke et al. 2009 contribution). For all other sources, we revert to the best-fitting Rieke et al. (2009) template without the additional AGN component.

4.5 'Value-added' IR properties catalogue

In Fig. 7 we provide a selection of SEDs to illustrate the observed data and the derivation of intrinsic properties. The examples originate from all six clusters (both central and parallel fields), are at varied redshifts (taken from spectroscopy, optical photometry and IR estimation) and exhibit a range of photometric completeness. An example of a source with a non-negligible AGN component is also included. Several of the most interesting SEDs are deliberately not shown in Fig. 7 as they are discussed individually in Section 5.

The derived intrinsic properties for all 263 *Herschel*–HFF sources are listed in Table 6. We defer the derivation of stellar masses to a later paper, when fully homogenized optical–IR SEDs are available. We remind the reader that the online version of this catalogue will be updated as further spectroscopic redshifts become available.

5 DISCUSSION

We now present a brief exploratory overview of the *Herschel*-detected population.

5.1 IR property distributions

Fig. 8 presents the distribution of three properties: redshift z, magnification μ and IR luminosity $L_{\rm IR}$. The distributions remain unchanged regardless of the inclusion of the sources with only an IR-estimated redshift, supporting their general validity.

In the z distribution, a broad peak at $z \sim 0.4$ dominates the central population, indicating a substantial population of cluster members. Indeed, 49 *Herschel* sources located in the central footprints have a cluster counterpart. In the parallel fields, there are only seven. Naively this suggests a prevalence of IR-bright cluster galaxies in the core, contradicting the notion that clusters effectively quench star formation (e.g. Fadda et al. 2008; Haines et al. 2015). However, there are several important factors we need to take into account. First, star-forming galaxies at the cluster redshift typically exhibit a dust peak in the PACS bands, and so they are less likely to be detected and/or well-constrained in the parallel fields with SPIRE imaging only. Secondly, line of sight projection means that the central footprints actually probe the full range of cluster radii, and it is virtually impossible to say whether a cluster source coincident with the core is truly at a low cluster-centric radius. Third, the number density of all cluster members (SF+quiescent) is much higher in the cluster core so the number count of SF members is a worse tracer of activity than e.g. the star-forming fraction (Haines et al. 2013). In total, 56/263 (21 per cent) IR-bright sources are identified as cluster members.

Figure 7. Example IR SEDs illustrating the observed photometry and fits. In each panel, observed (uncorrected) fluxes are shown by open circles: IRAC=cyan, MIPS=grey, *WISE*=green, PACS=blue, SPIRE=red. Non-detections (5σ upper limits) are denoted by a 'v'. Also plotted are the best-fitting modified-blackbody (grey dashes), Rieke et al. (2009) template (black solid line) and Berta et al. (2013) template (orange solid line). Derived IR properties from each of the two template sets (in matching colours) take into account the magnification, μ (shown to the right). Redshifts are spectroscopic (z_{spec}), optical photometric (z_{phot_opt}) or IR-derived (z_{phot_FIR}; see Section 4.4.1). For SEDs with a fitted AGN component, the two component model and star formation IR properties are shown in purple.

A further 44/263 (17 per cent) of the *Herschel* detections are in the cluster foreground, and are not discussed futher in this study.

The majority of *Herschel*-detected sources in HFF are beyond the cluster redshift (163/263; 62 per cent). They have a median redshift of $z = 1.0$. Two sources are at $z > 3$, while a further seven lie at $2 < z < 3$. As mentioned in Section 3.3, we may be bias against the faintest, highest-redshift sources, which would have an IR dust peak in the redder SPIRE bands. These source could be too faint for the bluer *Herschel* bands (PACS and even SPIRE 250 μm) meaning that they are unlikely to be detected in enough IR bands to be included in our catalogue. Additional imaging at longer wavelengths (e.g. JCMT/SCUBA-2, ALMA) increases the likelihood of identifying these sources, as illustrated by e.g. Boone et al. (2013) and also by the four highest redshift sources in our catalogue, which all have existing (sub)-millimetre photometry beyond SPIRE. We return to those four sources in Section 5.2.

While the number of $z > 1.2$ sources is roughly equal in central and parallel regions, the population of background galaxies at $z < 1.2$ is significantly larger in the inner fields. This is reflected in the median redshift of background sources: $z = 0.95$ in the centre and $z = 1.2$ for the parallel fields. This is likely to result from a combination of the limitations of detecting $z < 1$ sources without

Table 6. Optical counterparts for *Herschel*-detected sources within HFF. Derived properties account for magnification (μ).

ID[a]	Field[b]	Optical/NIR/radio counterpart				μ (ref)[e]	L_{IR}[f]	SFR_{IR}[f]	T_{dust}[g]	AGN[h]
		RA[c]	Dec[c]	(ref)[c]	z (ref)[d]		$\log(L/L_\odot)$	($M_\odot$ yr^{-1})	(K)	
HLSJ001412.7–302359	A2744 C	3.552819	−30.399785	(H)	**0.688** (1)	1.21 (1)	11.21 ± 0.09	18.3 ± 3.3	26.7 ± 1.6	0
HLSJ001415.3–302423	A2744 C	3.563939	−30.406277	(H)	**0.653** (1)	1.28 (1)	11.17 ± 0.09	16.7 ± 3.0	25.9 ± 1.5	0
HLSJ001416.7–302304	A2744 C	3.569295	−30.384239	(H)	**0.296** (1)	– –	10.16 ± 0.12	1.6 ± 0.4	19.8 ± 1.8	0
HLSJ001416.5–302410	A2744 C	3.568938	−30.402831	(H)	*∼0.5* (2)	1.30 (1)	10.88 ± 0.16	8.6 ± 3.2	27.7 ± 2.4	1
HLSJ001418.5–302246	A2744 C	3.577030	−30.379500	(H)	**0.498** (3)	1.40 (1)	10.90 ± 0.09	9.1 ± 1.6	26.3 ± 1.4	0
HLSJ001417.6–302301	A2744 C	3.573229	−30.383567	(H)	*∼0.9* (2)	1.95 (1)	11.97 ± 0.13	107.2 ± 31.4	23.0 ± 1.6	0
HLSJ001418.5–302448	A2744 C	3.576912	−30.413433	(H)	**1.366** (4)	1.68 (1)	11.86 ± 0.08	81.5 ± 14.7	31.7 ± 1.5	0
HLSJ001418.0–302529	A2744 C	3.575482	−30.424512	(I)	*∼3.5* (2)	1.42 (1)	12.64 ± 0.09	501.5 ± 105.5	27.7 ± 2.4	0
...	...	...	...	...	...	...	...	...	...	...

[*Notes.* The full table is published in the electronic version of the paper. A portion is shown here for illustration.]
[a] *Herschel* ID as in Table 4.
[b] C=central region; P=parallel.
[c] Counterpart RA and Dec, from the most accurate available position (V=VLA, H=*HST*, O=[ground-based] optical, I=IRAC, W=*WISE*, P=PACS, S=SPIRE).
[d] Counterpart **spectroscopic**, optical photometric or *IR-estimated* redshift from (1) Owers et al. (2011), (2) z_{phot_FIR}, (3) Couch et al. (1998), (4) Rawle et al. (2014a), (5) Wang et al. (2015), (6) Busarello et al. (2002), (7) Braglia et al. (2009), (8) Wold et al. (2012), (9) *HST* GRISM, (10) Bamford (2005), (11) Ivison et al. (1998), (12) Soucail et al. (1988), (13) Henry & Lavery et al. (1987), (14) Soucail et al. (1999), (15) Magellan/IMACS, (16) CLASH *HST* photo-z, (17) CLASH Subraru photo-z, Umetsu et al. (2014), (18) Balestra (2013), (19) Ebeling et al. (2014), (20) LBT/MODS, (21) Smith et al. (2009), (22) Walth et al. (in preparation), (23) Gómez et al. (2012), (24) Karman et al. (2015)
[e] $\mu$from (1) CATS models (Jullo & Kneib 2009; Jauzac et al. 2012; Richard et al. 2014; Jauzac et al. 2014) or (2) SaWLens wide-field method Merten et al. (2009, 2011). '–' for foreground and cluster sources.
[f] From the best-fitting Rieke et al. (2009) template.
[g] Characteristic dust temperature of the best-fitting single-temperature modified blackbody.
[h] Flag for alternate IR SED fit using SF+AGN model, effectively correcting L_{IR} and SFR_{IR} for AGN contamination (see Section 4.4.4).

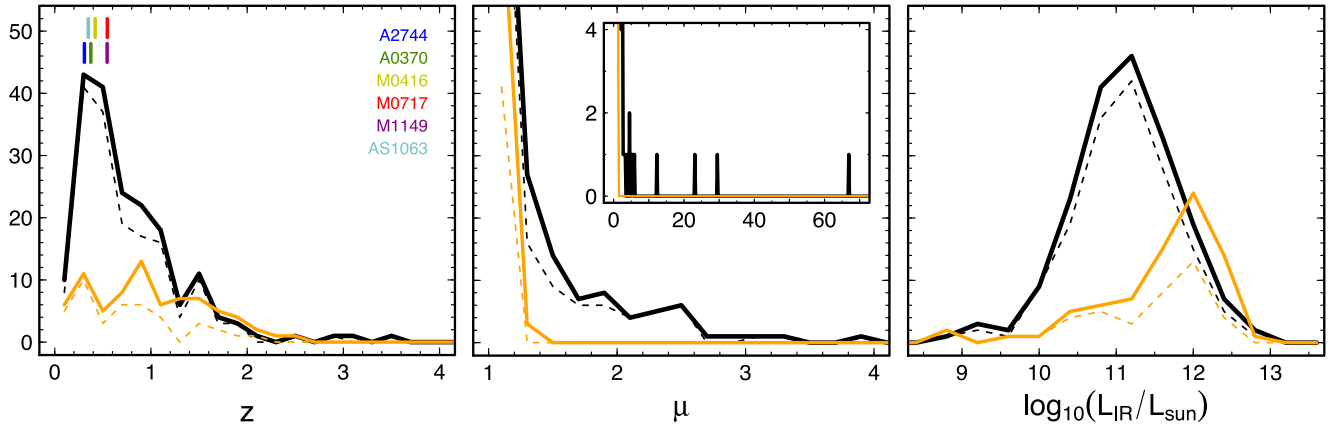

Figure 8. Property distributions for the *Herschel*-detected population, divided into central (black) and parallel (orange) regions, and either including (solid) or excluding (dashed) sources with only an IR-estimated redshift. Left-hand panel: redshift z, with cluster redshifts indicated by the coloured lines towards the top-left. Centre: magnification factor μ, with an inset panel showing $\mu > 4$. Right: total IR luminosity L_{IR}, corrected for magnification.

PACS (or *Spitzer*) coverage and also the increased lensing power within the central regions for the 'sweet spot' of magnification at $z \sim 1$.

For the background population, the median $\mu = 1.24$, rising to $\mu = 1.43$ for the 109 behind the central footprints, as all sources within parallel field undergo $\mu < 1.25$. The distributions in Fig. 8 clearly shows this difference, which is unsurprising as the critical lines of the cluster mass models all fall within those core regions. In total, 29 sources are more than doubled in brightness ($\mu > 2$).

The (magnification-corrected) L_{IR} distribution in the cores also peaks at lower intrinsic luminosity, which is entirely expected given what we know about the data, physics and galaxy population: 1) the magnification is stronger in the core, allowing us to see further down the luminosity function; 2) the lack of *Spitzer* and PACS imaging in the parallel fields decreases the effective detection limit; 3) the smaller population of objects in the cluster outskirts limits the number of nearby, intrinsically faint objects seen without lensing. In total, the background sample of 162 sources includes 99 LIRGs ($10^{11} < L_{IR} < 10^{12}$ $L_\odot$) and 23 sub-LIRGs ($L_{IR} < 10^{11}$ $L_\odot$).

Fig. 9 brings together all the previous information and effectively illustrates the benefits of lensing surveys by highlighting the most interesting sources. We can immediately see that the highest redshift sources ($z > 2$) are rare, and typically are not boosted from significantly below the nominal detection limit. The highest magnification, and intrinsically faintest background sources tend to be located within the redshift range $0.6 < z < 1.6$: more than 10 sub-LIRGs, and a similar number of LIRGs, all boosted from below the nominal detection limit.

We compare the HFF population to larger samples by exploring the L_{IR}–T_{dust} plane. Fig. 10 shows that sources from both HFF and

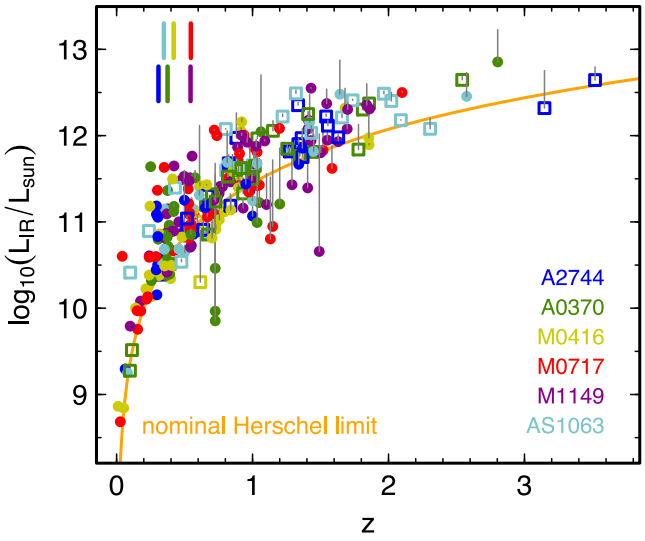

Figure 9. Magnification-corrected IR luminosity ($L_{\rm IR}$) versus the counterpart redshift for *Herschel*-detected sources in HFF. Closed circles are from the central regions and open squares from the parallel fields, colour-coded by the cluster (cluster redshifts are indicated by solid lines towards the upper-left). Grey vertical lines indicate the magnification effect for individual sources. The solid orange curve presents the nominal limit of the *Herschel* observations without lensing.

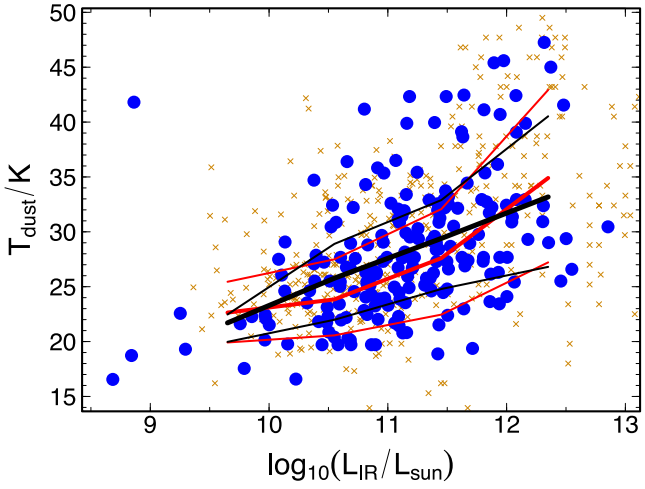

Figure 10. Magnification-corrected IR luminosity ($L_{\rm IR}$) versus the characteristic dust temperature ($T_{\rm dust}$) for HFF sources (blue filled circles). Those with only $z_{\rm phot\_FIR}$ are excluded. Black lines show the population trend (and ± 20 per cent percentiles). Comparison samples from Blain et al. (2003) and Hwang et al. (2010) (corrected to match $\beta = 2$) are shown by orange crosses, with the general trend displayed by red lines.

previous studies, e.g. Blain et al. (2003) and Hwang et al. (2010) (corrected to match $\beta = 2$), sample very similar parent populations. This emphasizes the obvious point: lensing is unlikely to select atypical sources, but rather allows us to observe larger numbers of 'normal' sources to a fainter limit.

An exploration of the morphology of the IR-bright population is beyond the scope of this paper. Although Table 6 offers a unique launch pad for a quantitative analysis of the optical counterparts (such as Mancini et al. 2015), we defer such an effort to future papers.

5.2 Highest redshift sources

We now briefly describe a few of the most interesting *Herschel*-detected sources within the HFF, starting with those at highest redshift. The four highest redshift sources are magnified by $\mu \sim 1.5 - 3$, but are all intrinsically bright ULIRGs ($L_{\rm IR} > 10^{12}$ L$_\odot$) magnified from near to, or above, the nominal *Herschel* limit (Fig. 11). In *HST* imaging, they are small, faint, red and point-like, as expected for high redshift sources without very strong magnification.

The two $z > 3$ sources, both located behind A2744, only have IR-derived redshift estimates. Fortunately, the $z_{\rm phot\_FIR}$ constraint is also aided by the 870 μm detection. Furthermore, *Spitzer* fluxes (unused in the redshift estimate) provide a good independent validation of a $z > 3$ continuum shape (upper panels, Fig. 11). These two sources are to be explored in more detail by Boone et al. (in preparation).

The highest redshift source in the sample with a confirmed spectroscopic redshift is HLSJ023951.9–013559 at $z = 2.803$ behind A370, which is better known as SMM02399–0136 (e.g. Ivison et al. 1998, 2010). We combine our *Herschel* fluxes with (sub)-millimetre continuum observations from JCMT/SCUBA at 450, 750, 850 μm and 1.35 mm (Ivison et al. 1998; Cowie, Barger & Knieb 2002), PdBI 1.27 mm (Genzel et al. 2003) and IRAM-30m/GISMO 2 mm. From a pure Rieke et al. fit, we derive an estimate of the SFR $= 1000 \pm 45$ M$_\odot$ yr^{-1} ($L_{\rm IR} = 10^{13.0}$ L$_\odot$) given $\mu = 2.37 \pm 0.08$. This agrees favourably with the PEP/HerMES catalogues by Magnelli et al. (2012) and the earlier estimate by Ivison et al. (1998), accounting for different magnification and IMF assumptions. However, the source is a well-known quasar host and exhibits an obvious power-law continuum in the mid-IR (Fig. 11, lower-left panel). Via the AGN fitting method described in Section 4.4.4, we derive an intrinsic SFR $= 812 \pm 35$ M$_\odot$ yr^{-1} ($L_{\rm IR} = 10^{12.85 \pm 0.02}$ L$_\odot$) and a characteristic dust temperature of 30.5 ± 0.7 K.

The final source displayed in Fig. 11 is located behind the AS1063 central footprint. The optical counterpart has an *HST*-derived photometric redshift from CLASH, which puts the source at $z = 2.57$ with a magnification of $\mu = 1.9$. We derive SFR $= 320 \pm 38$ M$_\odot$ yr^{-1} ($L_{\rm IR} = 10^{12.46 \pm 0.05}$ L$_\odot$) and $T_{\rm dust} = 25.5 \pm 1.7$ K. As with other IR-detected galaxies behind AS1063, this source will be explored further in Walth et al. (in preparation).

One conspicuous absence from our list of high-redshift sources in the HFF is the reported millimetre counterpart to the $z = 9.6$ candidate M1149-JD (Dwek et al. 2014). We do find a *Herschel* source (HLSJ114934.4+222446) within 10 arcsec of M1149-JD (Fig. 12), but this is entirely consistent with a nearby magnified spiral galaxy at $z \sim 1$ (Dwek et al. 2015; Zavala et al. 2015). The GISMO 2mm flux (0.4 ± 0.1 mJy) appears to be 0.5 dex higher than expected for that spiral, so M1149-JD may be dominant at 2 mm. However, any contribution by M1149-JD to the *Herschel* flux would be undetected, as shown by the theoretical dust SED in Fig. 12.

5.3 Strongest magnification sources

We now discuss several sources with the highest magnification. The 11 sources with $\mu > 4$ are listed in Table 7.

The most spectacular of the highly magnified sources is undoubtedly the strongly lensed arc ($z = 0.725$) in A370. This is well known as the original spectroscopically confirmed cluster-lensed arc (Soucail et al. 1988), and the dusty star-forming component was first glimpsed using the *Infrared Space Observatory* Camera (ISOCAM) by Metcalfe et al. (2003). The ~20 arcsec feature actually comprises

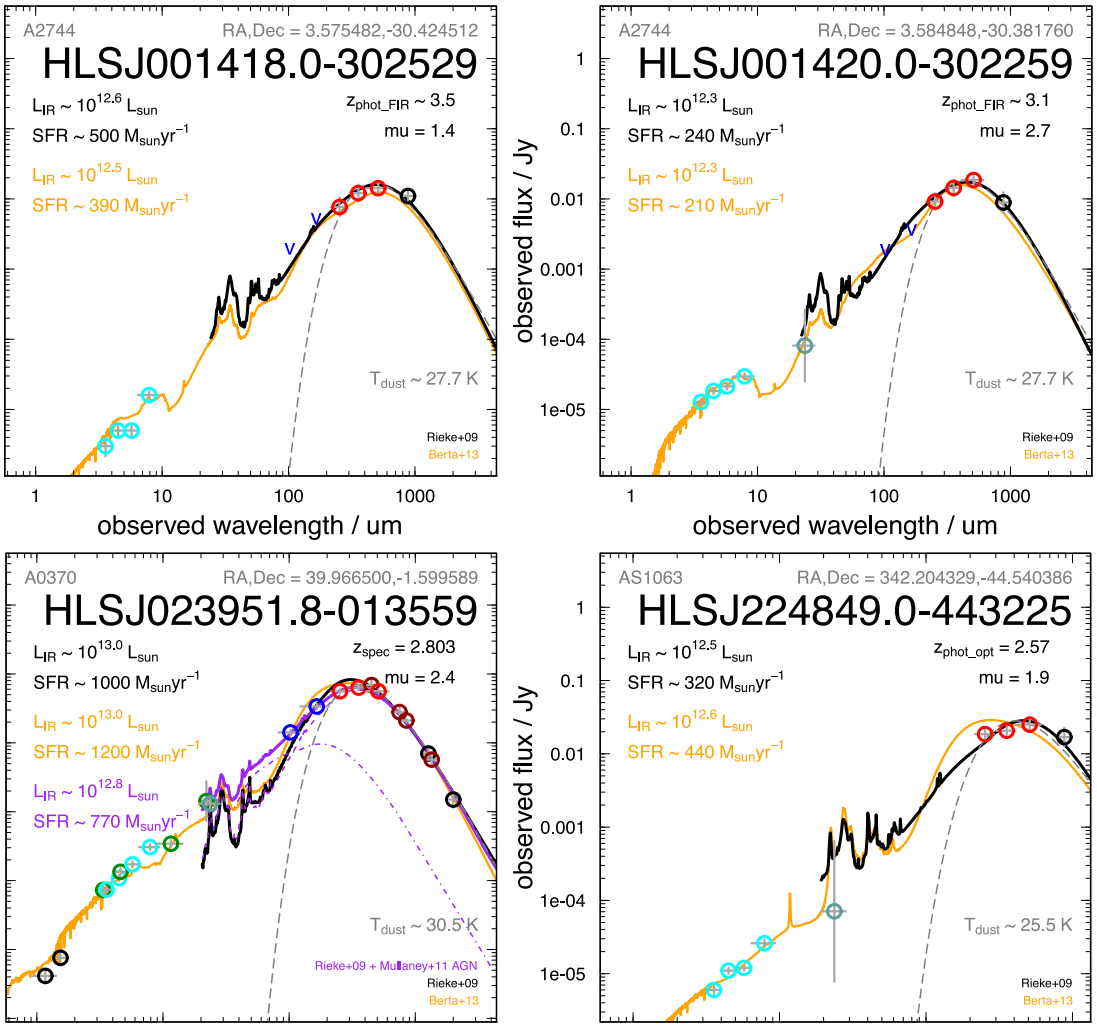

Figure 11. IR SEDs for the four highest redshift, *Herschel*-detected sources located in the HFF. Panel layout as in Fig. 7, with additional JCMT/SCUBA fluxes shown in brown and APEX/LABOCA, PdBI and IRAM-30m/GISMO continuum photometry in black.

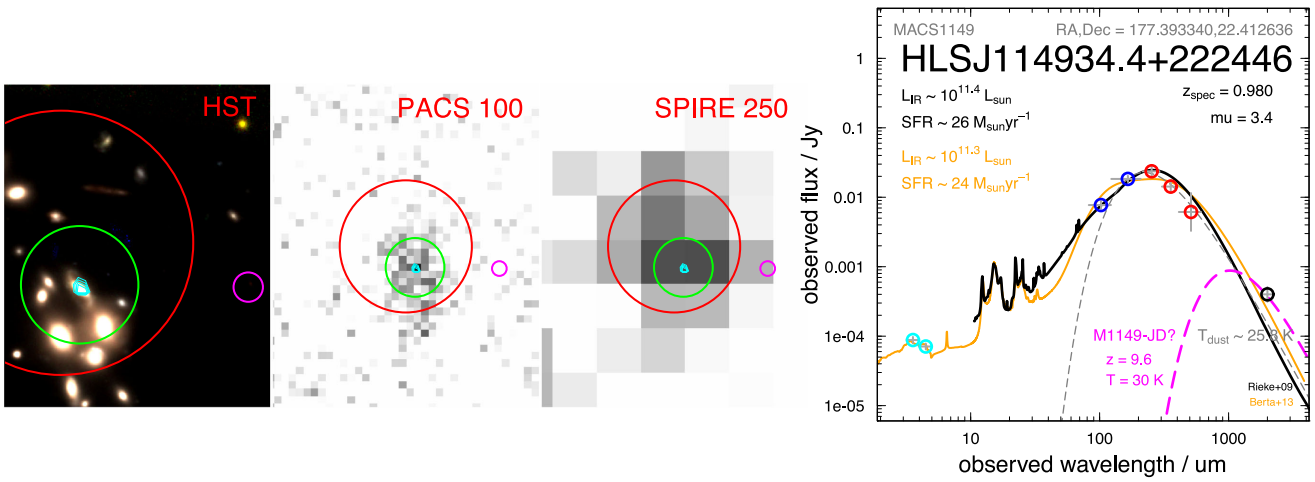

Figure 12. Left-hand panels: the $z = 9.6$ candidate M1149-JD (Dwek et al. 2014), marked by a 2 arcsec diameter magenta circle. Thumbnails show WFC3 1.05/1.25/1.60 μm, PACS 100 μm and SPIRE 250 μm. Green and red circles highlight the best-fitting PSF in PACS and SPIRE, respectively (diameters indicate PSF FWHM). Both originate from the $z \sim 1$ spiral galaxy, also detected by VLA (cyan contours). Right-hand panel: IR SED for the spiral galaxy (HLSJ114934.4+222446). Layout as in Fig. 7. A second dust SED (magenta dashes) shows that even if M1149-JD dominated the GISMO 2mm flux, it would not contribute significantly in the *Herschel* bands (assuming $T_{dust} = 30$ K).

Table 7. *Herschel*-detected sources with the highest magnification ($\mu > 4$).

ID	Cluster	z^a	μ^b	$\log(L_{\rm IR}/{\rm L}_\odot)^c$	Notes
HLSJ023953.0–013507	A0370	0.725	109 ± 16	10.09 ± 0.07	**Fig. 13.** Arc (e.g. Soucail et al. 1988) catalogued as three *Herschel* sources
HLSJ023952.6–013506					
HLSJ023953.7–013503					
HLSJ114935.5+222350	MACS1149	**1.491**	23.0 ± 7.0	10.66 ± 0.09	**Fig. 14.** Multiple-image supernova host (e.g. Smith et al. 2009)
HLSJ071734.4+374432	MACS0717	1.15	5.9 ± 0.8	10.95 ± 0.08	
HLSJ023952.0–013348	A0370	**1.034**	5.5 ± 0.4	10.99 ± 0.09	
HLSJ071736.8+374507	MACS0717	1.13	5.2 ± 0.7	10.80 ± 0.45	
HLSJ224841.8–443157	AS1063	**0.610**	5.1 ± 0.1	11.42 ± 0.08	Large spiral (Walth et al., in preparation)
HLSJ023956.6–013426	A0370	**1.062**	4.6 ± 0.3	12.04 ± 0.09	**Fig. 15.** Ring galaxy (e.g. Soucail et al. 1999)
HLSJ023954.1–013532	A0370	**1.200**	4.5 ± 0.2	11.21 ± 0.08	**Fig. 16.** Interlinked rings
HLSJ041607.7–240432	MACS0416	*∼0.6*	4.0 ± 0.1	10.30 ± 0.18	

[a]Counterpart redshift format as in Table 6.
[b]All magnification factors from the CATS models.
[c]$L_{\rm IR}$ corrected for magnification.

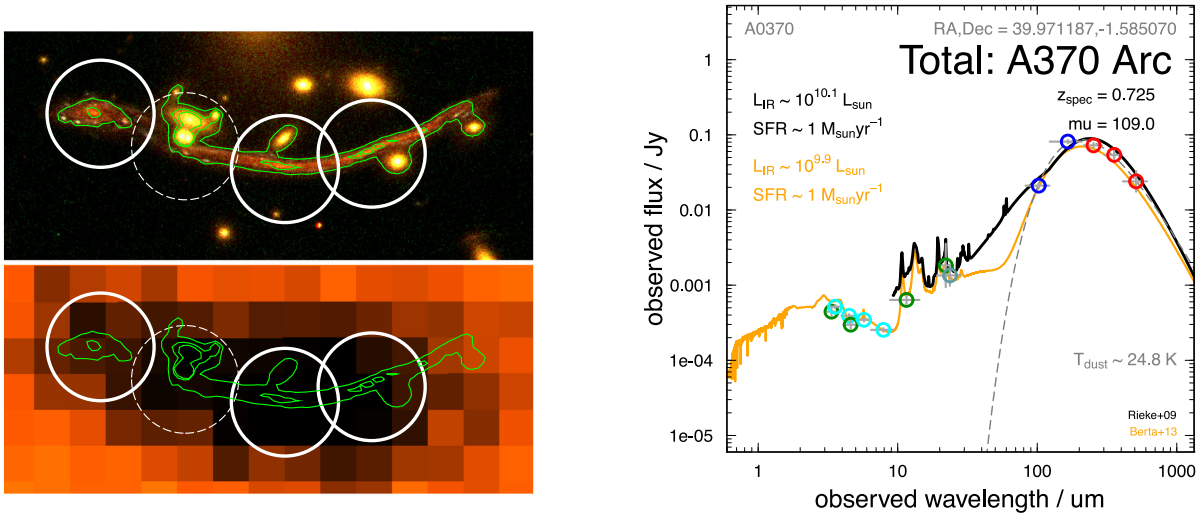

Figure 13. The strongly lensed arc at $z = 0.725$ behind A370. Left-hand panels: ACS 475/625/814 nm (upper) and PACS 100 μm (lower) maps of the arc (approximately outlined in green). The arc is catalogued as three separate *Herschel* sources (see Table 7) highlighted by solid white circles with 8 arcsec diameters (PACS PSF FWHM). A fourth IR source was only detected at 100 μm and is therefore cut from the catalogue (dashed circle). The western end of the optical arc is undetected by *Herschel*. Right-hand panel: IR SED summed over the whole arc, assuming a magnification $\mu = 109$. Panel layout as in Fig. 7.

five distorted images of the same background galaxy (Richard et al. 2010), as shown in the upper-left panel of Fig. 13.

The PSF fitting technique identifies four of the images as individual *Herschel* sources, although one is only detected at 100 μm and is cut from the final catalogue. The western end of the optical arc is too faint for detection in any *Herschel* band. The three catalogue sources are listed individually in the full Table 6. The uppermost rows of Table 7 give the total intrinsic properties of the arc summed over all five images, with the total SED presented in Fig. 13. Assuming a magnification $\mu = 109 \pm 16$, we derive a significantly sub-LIRG $\rm SFR_{total} = 1.40 \pm 0.05\ M_\odot\ yr^{-1}$ ($L_{\rm IR} = 10^{10.1}\ {\rm L}_\odot$) and a $T_{\rm dust} = 24.8 \pm 0.4$ K. Reassuringly, each of the individual images also exhibit the same SED shape and $T_{\rm dust}$.

The second source in Table 7, HLSJ114935.5+222350 behind M1149, is also widely known. The source corresponds to the highest magnification image ($\mu \sim 23 \pm 7$) of a lensed galaxy at $z = 1.49$, labelled A1.1 in Smith et al. (2009). This source recently became the first known host of a multiply imaged supernova, including a spectacular Einstein cross (Kelly et al. 2015). None of the other images are detected by *Herschel*. Fig. 14 presents the *HST*/WFC3 image and IR SED, which shows an intrinsically faint (sub-LIRG) source, with a $\rm SFR{=}5.1 \pm 0.9\ M_\odot\ yr^{-1}$ ($L_{\rm IR} = 10^{10.7 \pm 0.1}\ {\rm L}_\odot$) and a $T_{\rm dust} = 36 \pm 4$ K. Using Fig. 9, we confirm that this is one of the faintest galaxies in the survey, more than an order of magnitude below the nominal detection limit of *Herschel*.

HLSJ114935.5+222350 ($z = 1.49$) was studied in the compilation of 17 lensed sources by Saintonge et al. (2013), named 'J1149'. As the only overlap between the two samples, we briefly compare SEDs. The SPIRE photometry agrees perfectly (<5 per cent), which is well within the stated errors and should not be a surprise given the near identical data reduction and similar (PSF-fitting) flux derivation. Our PACS photometry in Table 4 is systematically higher (by ∼40 per cent), but the fluxes are very faint and very uncertain in both studies (between 50 and 100 per cent errors), so the 1–2 mJy difference between our results and Saintonge et al. (2013) can be explained by the noise. Our SED yields a higher SFR (5.16 ± 0.85 compared to $3.4 \pm 2.8\ \rm M_\odot\ yr^{-1}$), but both this property and $T_{\rm dust}$ agrees within the errors. We note that the extinction-corrected SFR derived from V_{555} by Smith et al. (2009) agrees better with our higher IR estimate (SFR ∼6 $\rm M_\odot\ yr^{-1}$).

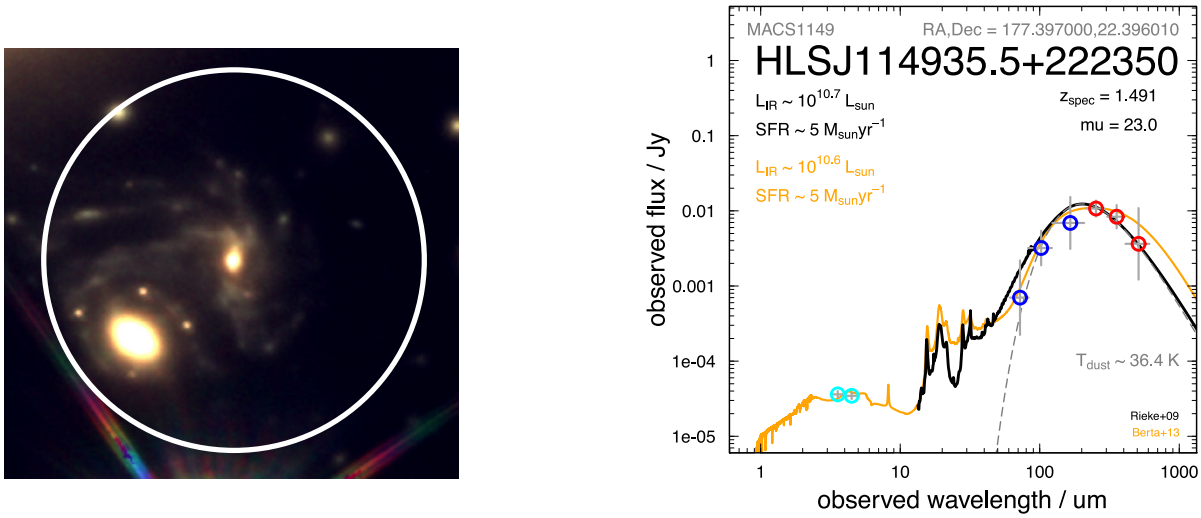

Figure 14. The strongly lensed ($\mu \sim 23 \pm 7$) supernova host at $z = 1.49$ behind M1149 (e.g. Smith et al. 2009; Saintonge et al. 2013). Left-hand panel: WFC3 1.05/1.25/1.60 μm image, including the supernova Einstein cross. The solid white circle indicates the location of the PACS detection, with an 8 arcsec diameter (PACS PSF FWHM). Right-hand panel: IR SED of this sub-LIRG (layout as in Fig. 7).

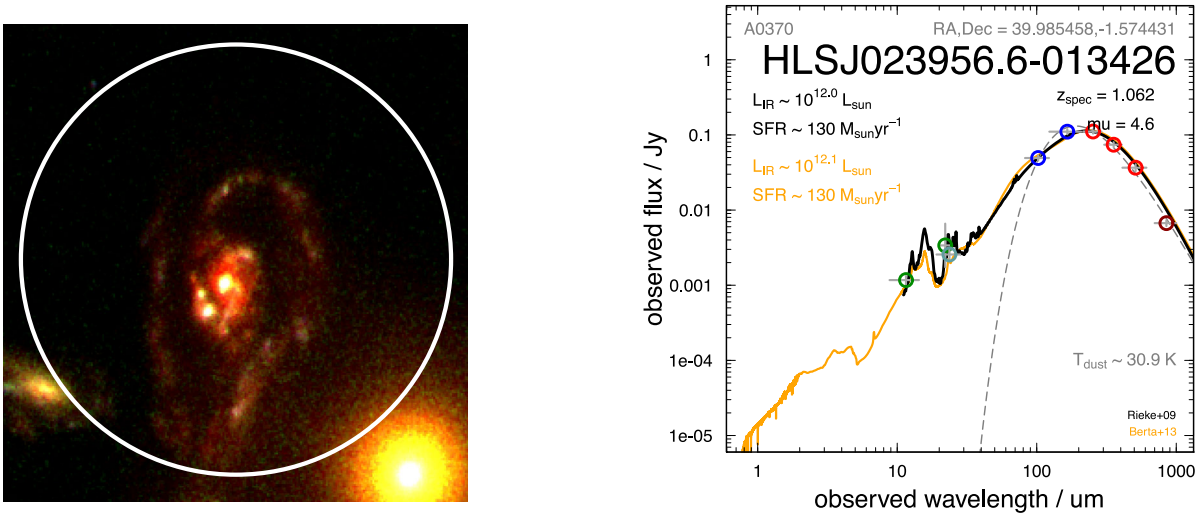

Figure 15. The magnified ($\mu = 4.6$) source HLSJ023956.6–013426 (SMMJ02399–0134; Smail et al. 1998; Soucail et al. 1999; Magnelli et al. 2012) at $z = 1.062$ behind A370. Layout as in Fig. 14 (but with *HST* 475/625/814 nm image).

Next we described the ring galaxy HLSJ023956.6–013426 at $z = 1.062$ behind A370 ($\mu = 4.6 \pm 0.3$), as shown in Fig. 15. The galaxy was extensively explored by Soucail et al. (1999), although previously detected as a SCUBA source (Smail et al. 1998, A370 L3). This distorted, ring-shaped source is one of the brightest *Herschel* point sources within the HFF footprints, and we calculate an intrinsic SFR $= 126 \pm 5$ $M_\odot$ yr^{-1} ($L_{IR} = 10^{12.04 \pm 0.01}$ $L_\odot$) and $T_{dust} = 31 \pm 1$ K. *Herschel* photometry (from the PEP/HerMES catalogue) has previously been published for this source (Magnelli et al. 2012, SMMJ02399–0134) allowing us another opportunity to check our derived properties. The authors applied a lower $\mu = 2.5$, but correcting for this, the derived properties are reassuringly similar: $L_{IR} = 10^{12.04 \pm 0.05}$ $L_\odot$ and $T_{dust} = 31 \pm 1$ K.

The next highest magnification source, HLSJ023954.1–013532 at $z = 1.20$ (from *HST* grism spectroscopy) behind A370 ($\mu = 4.5$), also has an interesting morphology, as shown in Fig. 16. The source has a magnification-corrected SFR $= 18 \pm 2$ $M_\odot$ yr^{-1} ($L_{IR} = 10^{11.21 \pm 0.04}$ $L_\odot$) and a typical $T_{dust} = 27 \pm 2$ K. This is a prime example of a $z > 1$ LIRG which has been magnified by cluster lensing to enable a very good constraint on the IR properties. Thus far, this galaxy has not been specifically targeted in any published observations.

The remaining strongly lensed sources are a mixed bunch of distorted spiral or irregular morphologies, including a sub-LIRG spiral galaxy just behind AS1063 (described further in Walth et al., in preparation) and several LIRGs at $z \sim 1$.

6 CONCLUSIONS

We present a complete census of the 263 *Herschel*-detected sources within the *HST* Frontier Fields, including 163 lensed sources located behind the clusters. Our primary aim is to provide a robust legacy catalogue of the *Herschel* fluxes, which we combine with archival data from *Spitzer* and *WISE* to produce IR SEDs.

We optimally combine the IR photometry with data from *HST*, VLA and ground-based observatories in order to identify optical

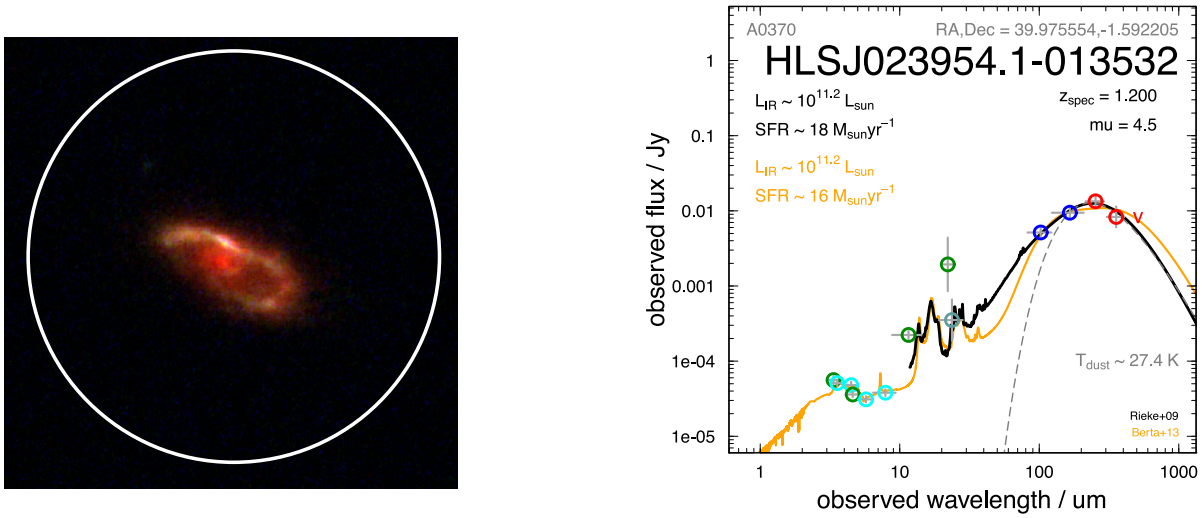

Figure 16. A magnified ($\mu = 4.5$) source at $z = 1.2$ behind A370. Layout as in Fig. 14 (but with *HST* 0.625/0.814/1.60 μm image).

counterparts and gain source redshifts. Hence we also provide a 'value-added' catalogue including magnification factor, intrinsic IR luminosity and characteristic dust temperature. We expect to update the derived properties for a few sources in the online catalogue, as (1) upcoming deeper/wider radio data helps to confirm our optical counterparts for sources without current VLA detections and (2) further spectroscopic observations secure the derived luminosity for the 151 sources without spectroscopic redshifts, particularly the 62 sources with only IR-based estimates. The catalogues will provide a useful reference for future multiwavelength studies of the HFF.

There are nine *Herschel* sources with counterparts at $z > 2$ and a further nine IR-bright sources with $\mu > 4$, six of which are sub-LIRG. Although we locate more than 20 background sub-LIRGs, it is clear that for an in-depth study of high-redshift, intrinsically faint sources, a larger cluster sample is required. Therefore, this work also serves as a preview of the full HLS (Egami et al. 2010), covering 10× the cluster sample, and many thousands of *Herschel*-detected sources (Egami et al., in preparation).

Herschel imaging, catalogues and source IR SEDs can be downloaded from the public flavour of the Rainbow Database.[10]

ACKNOWLEDGEMENTS

Herschel is a European Space Agency (ESA) space observatory with science instruments provided by European-led Principal Investigator consortia and with important participation from NASA. TDR was supported by an ESA Research Fellowship at the European Space Astronomy Centre (ESAC), in Madrid, Spain. RJI acknowledges support from the ERC in the form of the Advanced Investigator Program, 321302, COSMICISM. IRS acknowledges support from STFC (ST/L00075X/1), the ERC Advanced Investigator programme DUSTYGAL 321334 and a Royal Society/Wolfson Merit Award.

Based on observations made with the NASA/ESA *Hubble Space Telescope*, which is operated by the Association of Universities for Research in Astronomy, Inc., under NASA contract NAS 5-26555. These observations are associated with programmes #11689, 13389, 13495, 13496, 13498, 13504. This publication also uses data products from the *Wide-field Infrared Survey Explorer* (*WISE*), which is a joint project of UCLA and JPL, Caltech, funded by NASA. This research made use of the NASA/IPAC Infrared Science Archive, which is operated by JPL, Caltech, under contract with NASA.

We made use of a private version of the Rainbow Cosmological Surveys Database, operated by the Universidad Complutense de Madrid (UCM), and PGP-G acknowledges support from Spanish Government MINECO grant AYA2012–31277.

This work also utilizes gravitational lensing models produced by PIs Ebeling (CATS) and Merten & Zitrin, funded as part of the *HST* Frontier Fields program conducted by STScI. STScI is operated by the Association of Universities for Research in Astronomy, Inc. under NASA contract NAS 5-26555. The lens models were obtained from the Mikulski Archive for Space Telescopes (MAST).

[10] https://rainbowx.fis.ucm.es

REFERENCES

Balestra I., 2013, A&A, 559, 9
Bamford S. P., 2005, MNRAS, 361, 109
Berta S. et al., 2013, A&A, 551, 100
Béthermin M. et al., 2015, A&A, 573, 113
Blain A. W., Barnard V. E., Chapman S. C., 2003, MNRAS, 338, 733
Boone F. et al., 2013, A&A, 559, 1
Braglia F. G., Pierini D., Biviano A., Bhringer H., 2009, A&A, 500, 947
Busarello G., Merluzzi P., La Barbera F., Massarotti M., Capaccioli M., 2002, A&A, 389, 787
Casey C. M., Narayanan D., Cooray A., 2014, Phys. Rev., 541, 45
Clements D. L. et al., 2010, A&A, 518, 8
Combes F. et al., 2012, A&A, 538, 4
Coppin K E. K. et al., 2011, MNRAS, 416, 680
Couch W. J., Barger A. J., Smail I., Ellis R. S., Sharples R. M., 1998, ApJ, 497, 188
Cowie L. L., Barger A. J., Kneib J.-P., 2002, AJ, 123, 2197
da Cunha E. et al., 2013, ApJ, 766, 13
Dessauges-Zavadsky M. et al., 2015, A&A, 577, 50
Domínguez Sánchez H. et al., 2014, MNRAS, 441, 2
Dressler A. et al., 2011, PASP, 123, 288
Dwek E., Staguhn J., Arendt R. G., Kovacks A., Su T., Benford D. J., 2014, ApJ, 788, 30
Dwek E. et al., 2015, ApJ, 813, 119
Eales S. et al., 2010, PASP, 122, 499

Ebeling H., Ma C.-J., Barrett E., 2014, ApJS, 211, 21
Egami E. et al., 2010, A&A, 518, L12
Elbaz D. et al., 2011, A&A, 533, 119
Fadda D., Biviano A., Marleau F. R., Storrie-Lombardi L. J., Durret F., 2008, ApJ, 672, 9
Geach J. E. et al., 2015, MNRAS, 452, 502
Genzel R., Baker A. J., Tacconi L. J., Lutz D., Cox P., Guilloteau S., Omont A., 2003, ApJ, 584, 633
Gómez P. L. et al., 2012, AJ, 144, 79
Griffin M. et al., 2010, A&A, 518, L3
Haines C. P. et al., 2013, ApJ, 775, 126
Haines C. P. et al., 2015, ApJ, 806, 101
Henry J. P., Lavery R. J., 1987, ApJ, 323, 473
Huang J. S. et al., 2004, ApJS, 154, 44
Hwang H. S. et al., 2010, MNRAS, 409, 75
Ibar E. et al., 2010, MNRAS, 409, 38
Illingworth G. D. et al., 2013, ApJS, 209, 6
Ivison R. J., Smail I., Le Borgne J.-F., Blain A. W., Kneib J.-P., Bezecourt J., Kerr T. H., Davies J. K., 1998, MNRAS, 298, 581
Ivison R. J., Smail I., Papadopoulos P. P., Wold I., Richard J., Swinbank A. M., Kneib J.-P., Owen F. N., 2010, MNRAS, 404, 198
Jauzac M. et al., 2012, MNRAS, 426, 3369
Jauzac M. et al., 2014, MNRAS, 443, 1549
Jullo E, Kneib J.-P., 2009, MNRAS, 395, 1319
Karman W. et al., 2015, A&A, 574, 11
Kelly P. et al., 2015, Science, 347, 1123
Kelson D. D., 2003, PASP, 115, 688
Kennicutt R. C., Jr, 1998, ARA&A, 36, 189
Kroupa P., 2002, Science, 295, 82
Kümmel M., Walsh J. R., Pirzkal N., Kuntschner H., Pasquali A., 2009, PASP, 121, 59
Lutz D. et al., 2011, A&A, 532, 90
Magnelli B. et al., 2012, A&A, 539, 155
Magnelli B. et al., 2014, A&A, 561, 86
Mancini C., Renzini A., Daddi E., Rodighiero G., Berta S., Grogin N., Kocevski D., Koekemoer A., 2015, MNRAS, 450, 763
Merten J., Cacciato M., Meneghetti M., Mignone C., Bartelmann M., 2009, A&A, 500, 681
Merten J. et al., 2011, MNRAS, 417, 333
Metcalfe L. et al., 2003, A&A, 407, 791
Mullaney J. R., Alexander D. M., Goulding A. D., Hickox R. C., 2011, MNRAS, 414, 1082
Nguyen H. T. et al., 2010, A&A, 518, L5
Oliver S. et al., 2012, MNRAS, 424, 1614
Ott S., 2010, ASP Conf. Ser., 434, 139
Owers M. S., Randall S. W., Nulsen P. E. J., Couch W. J., David L. P., Kempner J. C., 2011, ApJ, 728, 27
Pappalardo C. et al., 2015, A&A, 573, 129
Pearson E. A. et al., 2013, MNRAS, 435, 2753
Pereira M. J. et al., 2010, A&A, 518, 40
Pérez-González P. G. et al., 2008, ApJ, 675, 234
Pérez-González P. G. et al., 2010, A&A, 518, 15
Piazzo L., Ikhenaode D., Natoli P., Pestalozzi M., Piacentini F., Traficante A., 2012, IEEE Trans. Image Process., 21, 3687
Piazzo L., Calzoletti L., Faustini F., Pestalozzi M., Pezzuto S., Elia D., di Giorgio A., Molinari, S., 2015, MNRAS, 447, 1471
Pilbratt G. et al., 2010, A&A, 518, L1
Poglitsch A. et al., 2010, A&A, 518, L2
Postman M. et al., 2012, ApJS, 199, 25
Rawle T. D. et al., 2010, A&A, 518, 14
Rawle T. D. et al., 2012, ApJ, 747, 29
Rawle T. D. et al., 2012, ApJ, 756, 106
Rawle T. D. et al., 2014a, MNRAS, 442, 196
Rawle T. D. et al., 2014b, ApJ, 783, 59
Rex M. et al., 2010, A&A, 518, 13
Richard J., Kneib J.-P., Limousin M., Edge A., Jullo E., 2010, MNRAS, 402, L44
Richard J. et al., 2014, MNRAS, 444, 268
Riechers D. A. et al., 2013, Nature, 496, 329
Rieke G. H., Alonso-Herrero A., Weiner B. J., Pérez-González P. G., Blaylock M., Donley J. L., Marcillac D., 2009, ApJ, 692, 556
Rodighiero G. et al., 2014, MNRAS, 443, 19
Rowlands K. et al., 2014, MNRAS, 441, 1017
Saintonge A. et al., 2013, ApJ, 778, 2
Santini P. et al., 2014, A&A, 562, 30
Schmidt K. B. et al., 2014, ApJ, 782, 36
Schreiber C. et al., 2015, A&A, 575, 74
Sklias P. et al., 2014, A&A, 561, 149
Smail I., Ivison R. J., Blain A. W., 1997, ApJ, 490, 5
Smail I., Ivison R. J., Blain A. W., Kneib J.-P., 1998, ApJ, 507, 21
Smith G. P., Pontoppidan K. M., Young E. D., Morris M. R., van Dishoeck E. F., 2009, ApJ, 707, 163
Soucail G., Mellier Y., Fort B., Mathez G., Cailloux M., 1988, A&A, 191, L19
Soucail G., Kneib J. P., Bézecourt J., Metcalfe L., Altieri B., Le Borgne J. F., 1999, A&A, 343, 70
Speagle J. S., Steinhardt C. L., Capak P. L., Silverman J. D., 2014, ApJS, 214, 15
Swinbank A. M. et al., 2012, MNRAS, 427, 1066
Thomson A. P., Ivison R. J., Owen F. N., Danielson A. L. R., Swinbank A. M., Smail I., 2015, MNRAS, 448, 1874
Umetsu K. et al., 2015, ApJ, 795, 163
Walter F. et al., 2012, ApJ, 752, 93
Wang X. et al., 2015, ApJ, 811, 29
Wold I. G. B., Owen F. N., Wang W.-H., Barger A. J., Keenan R. C., 2012, ApJS, 202, 2
Wright E. L. et al., 2010, AJ, 140, 1868
Zavala J. A. et al., 2015, MNRAS, 453, 88
Zitrin A. et al., 2009, MNRAS, 396, 1985

SUPPORTING INFORMATION

Additional Supporting Information may be found in the online version of this article:

Table 4. Observed PACS and SPIRE fluxes for *Herschel*-detected sources within the *HST* Frontier Fields.
Table 6. Optical counterparts for *Herschel*-detected sources within HFF. Derived properties account for magnification (μ).
(http://www.mnras.oxfordjournals.org/lookup/suppl/doi:10.1093/mnras/stw712/-/DC1).

Please note: Oxford University Press is not responsible for the content or functionality of any supporting materials supplied by the authors. Any queries (other than missing material) should be directed to the corresponding author for the article.

This paper has been typeset from a TEX/LATEX file prepared by the author.